MODELING THE SOFT X-RAY BACKGROUND WITH MULTIPLE SUPERNOVAE

by

RANDALL K. SMITH

A dissertation submitted in partial fulfillment of the

requirements for the degree of

Doctor of Philosophy

(Physics)

at the

UNIVERSITY OF WISCONSIN — MADISON

1996

ABSTRACT

The existence and isotropy of the soft X-ray background is discussed, and explored, using a one-dimensional hydrocode with non-equilibrium cooling, multiple explosions, and dust. Analytical results derived from thermal conduction and Kahn cooling are compared with the results from the hydrocode. The temperature in a hot bubble of gas evolving under these conditions is found to be a simple function of radius,

$$T(r) = T_{central}(1 - (r/R_{shell})^2)^{2/7}.$$

Using this relation, the equilibrium emission is found for a bubble of radius 70-100 pc. Multiple explosions are found to be able to easily create such large bubbles, and the results also predict that the emission would be proportional to bubble radius, which agrees with one explanation of the X-ray — N_H anti-correlation. In order to match the observed emission, however, the pressure in the bubble must be at least 16,500 cm^{-3}K.

Acknowledgements

No man is an island, and no dissertation is a solo effort. Many people helped me throughout my career; I would like to thank them for their advice, criticism, and presence.

I would like to thank my thesis advisor, Don Cox, for his help throughout this process, beginning with encouraging me to come to Wisconsin, and with selecting a thesis topic, and many, many times in between.

My parents, Timothy and Jane Smith, for encouragement beginning with learning to count by 3s.

Irv Zigler, for retaining and showing me the joy of mathematics after having taught it to high school students for many years. David Stoutamire for many interesting discussions.

Eli Dwek, for convincing me to join this field by presenting a curious little geometry problem to me.

I would also like to thank Dick Edgar, Wilt Sanders, John Mathis, Dan McCammon, and Ron Reynolds for their help here at UW-Madison in my understanding of astrophysics and the interstellar medium.

Finally, many thanks to my fiancèe Lauren Boice, who not only gave moral support during this adventure, but also learned enough about my research to provide a critical eye reading my proposals and this thesis!

To the everlasting memory of $\Pi\alpha\lambda\lambda\grave{\alpha}\sigma$ $\acute{A}\theta\acute{\eta}\nu\eta$ and $T\acute{\upsilon}\chi\eta$, and to the $\omega\iota\sigma\pi$ oracle (and their respective corporate counsels).

Contents

List of Figures

List of Tables

Chapter 1

Soft X-Ray Background (SXRB) Data

1.1 Introduction

The sky above the Earth's atmosphere is bright in photons with energies between 0.1 and 1 keV, commonly called the soft x-ray background (SXRB). Understanding the origin and evolution of this emission has been the premier problem of diffuse x-ray astronomy in the last 20 years. In order to understand the physical processes creating the SXRB, to construct a model to explain its main features, it is of course necessary to examine in detail the observations and measurements of the SXRB. Thus a short historical overview is appropriate, to show how the field has evolved, as well as to extract those elements which characterize the SXRB. What follows is by necessity brief; the reader is recommended to the much more thorough reviews by McCammon & Sanders (1990) of the observational data on the SXRB and Cox and Reynolds (1987) on theories of the local interstellar medium. And, at the same time, it should be remembered that no general model could explain each and every feature of the SXRB described herein, since there will inevitably be idiosyncratic features and anomalies in reality. The goal is to create a model that explains the gross features, and to show how variations in the model might lead to the

variations seen in the data.

1.1.1 Early Observations

Diffuse isotropic X-rays were seen in the first observations of the 2-6 keV band (Giacconi *et al.* 1962). At these energies, the galaxy is transparent so the isotropy implies an extragalactic cosmological source. At lower energies the galaxy is not transparent, and if the extragalactic flux continued, observations below 1 keV would give information about the distribution of matter in the galaxy via x-ray shadowing. As a result of this hypothesis, there developed a great interest in soft x-rays and a number of groups built detectors to observe them: Bowyer *et al.* (1968), Henry *et al.* (1968), and Bunner *et al.* (1969) among others. While each group used its own instrument, all the instruments used gas-filled proportional counters as detectors, usually with Mylar filters. These filters transmit soft X-rays up to the carbon K-edge at 0.284 keV. Harder X-rays can penetrate but can be distinguished from the softer X-rays even with the limited energy resolution of the proportional counter. Thus, the experiments all had at least two energy bands, a soft one around 0.25 keV called the C band and a harder band around 0.50 keV called the M band. Since these experiments were flown on sounding rockets, they had limited data, yet they all found substantial emission in the soft C band. Bowyer *et al.* interpreted this as the partially absorbed continuation of the previously observed harder component, but noted that the absorption implied by the data was smaller than expected. Henry *et al.* also saw this emission and suggested that the excess at 0.25 keV was due to bremsstrahlung from an intergalactic plasma. Bunner *et al.* used two different types of filters (Mylar and Kimfol)

with different responses to get some spectral information about the 0.25 keV X-rays. With this data they determined that the SXRB was unlikely to be either from absorption or bremsstrahlung, and suggested that it might be due to unresolved population II stars.

Rocket flights continued and the group at Wisconsin led by W. L. Kraushaar began an all-sky mapping program with their instrument, which contained a C band filter and a Boron (or B band) filter cutting off energies above 0.188 keV. Williamson *et al.* (1974), one of the papers written for this project, concluded on the basis of the current data that the soft x-ray background must be due to line emission from ions in a hot plasma if it is the result of any normal astrophysical emission since all other known processes that emit X-rays have other effects that would have been observed. The hot plasma model had no disastrous consequences and tended to fit the emission data adequately with a temperature of $\sim 10^6$ K. Combined with the theoretical work of Cox & Smith (1974), who showed that the ISM could contain a widespread network of such hot plasma due to long-lived supernova remnants, these results were to inspire observational searches for the predicted ions and theoretical efforts to understand the creation and evolution of the hot plasma.

1.1.2 Copernicus

The hot plasma mechanism for the SXRB emission was supported by results from the Copernicus satellite, specifically observations of O VI, a tracer of hot gas, towards many stars (Jenkins & Meloy 1974). This O VI did not appear to be associated with the stars themselves but rather existed in clumps throughout the interstellar medium (ISM), suggesting large portions

of the ISM are in a hot gas phase. Jenkins analyzed the complete Copernicus dataset in a series of papers (Jenkins 1978a,b,c), concluding that the O VI was in clumps with an average column density per clump of 10^{13} cm^{-2}. The data were recently reanalyzed by Shelton & Cox (1994), adding the possibility of a local component to the model. They inferred the existence of a local component to the O VI data, likely to be in a shell of about 100 pc radius around the Sun with a velocity less than 10 km/s. They also found that the remaining O VI clumps are larger and less frequently encountered on average than Jenkins' result, with column densities of $2 - 7 \times 10^{13}$ cm^{-2}. This result will provide a useful constraint to the models considered later.

1.1.3 All-sky Surveys and Beyond

The next important observational step was the completion of the all-sky mapping program of the SXRB. Two satellites, HEAO-1 (Garmire *et al.* 1992) and SAS 3 (Marshall & Clark 1984), as well as the Wisconsin Sounding Rocket survey (McCammon *et al.* 1983), all created maps of the sky in the C band, and the Wisconsin survey also included a B band map. All 3 of the surveys agreed that there was significant anisotropy to the SXRB, with strong emission towards the halo of the Galaxy but only about 30% as much in the Galactic plane. They also found a significant anti-correlation between the B and C bands and neutral hydrogen column density when $N_{H\mathrm{I}} < 5 \times 10^{20}$cm^{-2}. Figure 1.1 shows this effect in the Wisconsin survey data (McCammon 1995, private communication). A fit can be made to the C band data of the form

$$C_{total} = C_{fg} + C_{bg} exp(-N_H \sigma) \tag{1.1}$$

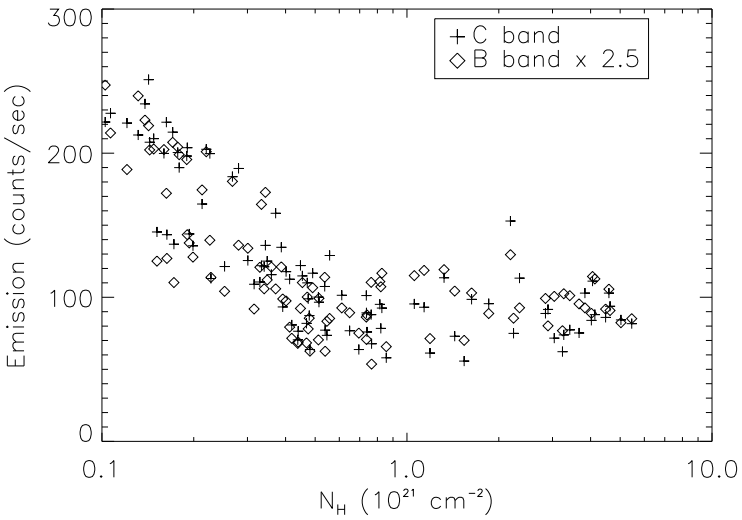

Figure 1.1: B (x 2.5) and C band emission versus column density

where σ is the effective cross section for absorption. In this case, the total emission consists of a foreground unabsorbed component C_{fg} of about 100 counts/second and a larger absorbed component C_{bg}. However, X-ray absorption is strongly energy-dependent ($\sigma(E) \propto E^{-3}$) and the ratio of the softer B band to the C band in all directions is nearly constant at 2.5; certainly there is no evidence in Figure 1.1 that the B band is more strongly absorbed than the C band. In addition, McCammon *et al.* (1983) found it "very difficult to reconcile ...[absorption] models ...with existing 21 cm observations [of the small scale distribution of absorbing neutral hydrogen]."

The Wisconsin group then built the Ultrasoft X-ray Telescope (UXT) which included a beryllium filter (Be band) with a strong absorption edge at 0.111 keV, even softer than the B band. Although a column density of only $N_H \sim 10^{18}$ cm^{-2} would have shown absorption, no such effect was seen in the Be band in any of the 3 flights of the instrument, which covered ∼10% of the

sky. These results allow limits to be placed on the amount and variation in any intervening material: no more than $\sim 7 \times 10^{18}$ cm^{-2} along an average line of sight (Juda *et al.* 1991) with the variations in the amount of absorbing material less than 2×10^{18} cm^{-2} (Bloch *et al.* 1986). In these observations, the Be band brightness correlated well with those of the B (and thus C) bands. These results require a local origin for a large fraction of the soft X-rays, and thus strongly constrain models of the SXRB.

1.1.4 ROSAT

The next all-sky survey to be completed was done by the German x-ray observatory named *Röntgensatellit*, or ROSAT. The satellite has three instruments, the High-Resolution Imager (HRI), the Position-Sensitive Proportional Counter (PSPC) and the Wide Field Camera (WFC) (Trümper 1983). The PSPC has $\lesssim 1$ arc minute resolution and a 0.1 – 2.0 keV response with moderate ($E/\Delta E \sim 1$ at 1/4 keV) energy resolution (Snowden *et al.* 1994a). The WFC is an extreme ultraviolet/soft X-ray instrument, operating between 80–150 Å(0.083 - 0.155 keV). The satellite scanned the entire sky with both instruments during 1990-1991.

The first publication of the PSPC survey results by Snowden *et al.* (1995) covered 98% of the sky with $\sim 2^\circ$ angular resolution, which is substantially better than any previous survey and renewed searches for absorbing clouds in the ISM. The results were presented in 3 bands, covering 1/4 keV, 3/4 keV, and 1.5 keV. The results agree with previous surveys, although there is an unknown source of contamination known as "Long Term Enhancements" which may not be fully removed from the 1/4 keV band. The survey shows, in

the ROSAT-equivalent of the C band, a wealth of structure and particularly when compared against maps of Galactic N_H, there is "almost ubiquitous negative correlation" (Snowden *et al.* 1995). This confirms the previous anti-correlation results; however, the anti-correlation is not perfect. For example, the region of minimum Galactic N_H is not a region of maximum x-ray emission (Snowden *et al.* 1994).

The increased angular resolution of the PSPC meant searches for x-ray shadows could now be done on individual clouds. Previous work searching for the shadow of the Small Magellenic Cloud against an assumed extragalactic source of soft X-rays found nothing (McCammon *et al.* 1971). The ROSAT results were negative in some directions. In low Galactic latitude ($|b| < 30°$) directions no shadows were seen, except for a shadow in the C band towards an enhancement associated with Loop I or the Galactic bulge and it is not "representative of the general diffuse background." (Burrows & Mendenhall 1994) At high latitudes, while no shadow in the C band was seen towards the nearby cloud MBM 12, 60–70 pc distant (Snowden *et al.* 1993), they were definitely seen towards some clouds. The Draco cloud, thought to be more than 200 pc above the plane of the Galaxy, shows clear evidence of shadowing (Snowden *et al.* 1991; Burrows & Mendenhall 1991). As a result, previous models of the SXRB as a purely local phenomenon, based on UXT and earlier observations, must now be modified since there is strong evidence for some halo (and/or extragalactic) emission. But this does not mean a return to the original halo models, since it is clear that this high latitude emission is very patchy. Observations through the Lockman hole, the lowest column density sightline out of the Galaxy show substantially *less* emission coming

from the halo in this direction compared to that coming from the Draco region. (Snowden *et al.* 1994) Nonetheless, in some directions, a portion of the C band X-rays are coming from beyond the local region.

1.1.5 DXS

In 1974, Williamson *et al.* suggested that high spectral resolution data would be necessary in order to observe the predicted emission lines. In 1993 the Diffuse X-ray Spectrometer (DXS) flew on the Space Shuttle and was the first soft X-ray (0.150 – 0.284 keV) experiment with sufficient spectral resolution ($E/\Delta E \sim 20$ to prove that the SXRB is not dominated by a smooth continuum but is rather a lumpy, line-filled spectrum (Sanders & Edgar 1995). The total emission is consistent with previous measurements in this direction, but the spectrum cannot be fit by any single-temperature plasma model with any set of elemental abundances. A fit can be obtained with a two-temperature model, but this fit would exceed the observed emission in the M band. Blast wave models similar to those which will be presented later have also been tried without success. It is probable that the problems with fitting the data are due at least partially to the plasma models themselves. These models rely on atomic data which are extremely difficult to measure in the laboratory or estimate using atomic theory. Fundamentally the DXS results are not currently well understood except that they show line emission.

1.1.6 EUV

Closely related to soft X-rays is the extreme ultraviolet (EUV), defined as the spectral range between 0.0136 keV and 0.1 keV (912Å– 124Å). At 0.1 keV, one optical depth is just an N_H of $1.8 \times 10^{19}\mathrm{cm}^{-2}$, and this decreases with increasing wavelength. If the nearby ISM had an average density of 1 cm^{-3}, 0.1 keV photons could travel only $\sim$ 6pc. Since the beginning of soft x-ray astronomy, the low energy photons observed have required a "close" source, which has gotten closer the lower the energies measured. Paresce (1984) used this effect and examined the column densities to nearby stars, using UV and EUV measurements as well as other methods, and concluded that the local ISM within $\sim$ 100 pc has an average density $\overline{n_H} = 0.07$ cm^{-3}. With only 82 stars in his survey and only 31 within 100 pc, his results were necessarily limited although they still show that the local ISM has lower density than the average. Most importantly for this project, this method provides a measurement of the local ISM characteristics independent of the soft X-ray background.

Much other work using the EUV to study the local ISM has been done and this picture has been generally confirmed; see Cox & Reynolds (1987) and references therein. Most recently, the third instrument on ROSAT, the WFC, created an all-sky map in EUV emission with a spectral range of $\sim 0.080-0.155$ keV ($\sim 80 - 150$Å). Using the 384 sources identified, mostly white dwarfs and late-type stars, Warwick *et al.* (1993) mapped the local N_H, found that the data were consistent with a there being a local cavity of average radius 80 pc and gas density of ~ 0.05 cm^{-3}, with denser regions surrounding the volume. Moreover, 0.025 cm^{-3} for the cavity density provided an "excellent fit" as well, and in fact the data did not support a strict lower bound to the density within

the volume. Subsequent work by Diamond *et al.* (1995) using the same data found evidence for a small region (within 20-30 pc) around the sun with density 0.1 cm^{-3}, and then a larger volume with radius 70 pc which has "negligible" neutral hydrogen, outside of which the density rises rapidly. In summary, clear evidence for lower density regions surround by "walls" of material at 70–100 pc exists in measurements of the column densities measured towards nearby stars.

1.1.7 Summary

Despite the inherent difficulty of observing the SXRB, there is actually enough information about it to draw a number of conclusions, albeit somewhat contradictory ones. The emission is brightest at high latitudes, and drops to 30% of the maximum value at the Galactic plane. There is a strong anti-correlation, even along lines of constant latitude, between the emission and N_H. While measurements of N_H in this anti-correlation vary from $5 \times 10^{18} - 5 \times 10^{20}$ cm^{-2}, the limit on the amount of absorbing material inside the emitting region is typically $\sim 7 \times 10^{18}$ cm^{-2}(Juda 1991). The broad band spectrum is fit by that of an unabsorbed 10^6 K plasma, and is largely due to lines, even though the higher resolution data from DXS is not fit by a 10^6 K plasma with any set of abundances. At low Galactic latitude, only one C band shadow has been seen, and that one in a peculiar direction. However, since shadows have been seen in the C band towards a few clouds in the halo of our Galaxy which are at least 200 pc above the plane, some of the C band has to be non-local in high latitude directions.

Clearly, no simple model could fit these data. However, there are three

aspects that can be considered necessary components to any interpretation of the local ISM and its contribution to the SXRB:

- There is a hot ($\sim 10^6$ K) plasma surrounding the Sun.
- This plasma creates nearly all of the SXRB seen towards the galactic plane, and a significant fraction of that seen at high latitude.
- The hot region is limited in scope, ending some 70–100 pc from the Sun in typical low latitude directions, though even the local component may extend considerably farther for $b \gtrsim 30^\circ$.
- The emission from the hot region is not isotropic; although cloud shadows are seen in the SXRB at high latitudes, the foreground emission in these directions is still greater than the emission in the plane.

1.2 Theoretical Models and Their Evolution

We now turn from the observations of the local ISM to the theories explaining these observations. These theories have evolved simultaneously with the observations, of course, so separating them is difficult. Models explaining the SXRB and the local ISM can largely be categorized within one of a few families, and at various times various families have been prominent. Unlike the relatively straightforward progress of data collection and analysis, theoretical understanding naturally tends to drift, with truth at times seeming just upon the threshold and then suddenly slipping out of sight.

1.2.1 Extragalactic

The hard X-ray background (2-10 keV) is isotropic, and the galaxy is transparent at these wavelengths, so this background must be extragalactic since the galactic plane is not visible (McCammon & Sanders 1990). The spectrum of this background has been fit to a power-law spectrum, $\sim (8-11)E^{-0.4}$ keV/(cm^2 s sr keV) (Marshall *et al.* 1980). Recent results have shown that much of this background is due to unresolved point sources, most likely active galactic nuclei, although some portion of it remains of unknown origin (Fabian & Barcons 1992). We do know that the SXRB at 0.25 keV cannot be simply this power-law spectrum continued down to lower energies, since this spectrum would be completely absorbed in the plane. In addition, in high latitude directions the observed emission is more than twice the extrapolated background. As stated above, ROSAT has observed for the first time some absorption by halo clouds, but this does not change the previous conclusion from the B and C band surveys and Be band data. These show no evidence for any absorption, and in fact strongly limit the amount of material between us and most of the emission. Yet the SXRB correlates inversely with N_H; if this cannot be absorption, it must be explained in some other fashion.

1.2.2 Displacement

If the emission cannot be behind the neutral hydrogen, it must be in front of it. Matching this idea with the observed anti-correlation led to the displacement model of the SXRB, where the X-rays are generated inside a large cavity, approximately 100 pc in radius, filled with hot gas (Sanders *et al.* 1977; Fried

Table 1.1: Displacement Model Parameters

Quantity	Removed	Swept Out
Electron density (cm^{-3})	0.0047	0.0037
Plasma Temperature (K)	$10^{6.0}$	$10^{6.0}$
Thermal Pressure ($cm^{-3}K$)	9000	7100
Stored Energy (ergs)	3.7×10^{50}	11.3×10^{50}
Volume Luminosity (ergs s^{-1})	5.1×10^{35}	12.1×10^{35}

et al. 1980). This cavity is a feature of most models of the local ISM, and is often called the "local bubble." Initial evidence for this bubble comes from the UV results, which measure an extremely low N_H column density towards many nearby stars. In the displacement model, the local bubble is then filled with gas uniformly emitting X-rays; variations in the SXRB emission are due to varying distances to the edge of the cavity. If the distance to the edge of the cavity is longer than average, the emission, assuming a constant emission per parsec will be greater than average. The anti-correlation with neutral hydrogen relies upon the fact that the scale height of the neutral hydrogen in the galaxy is about 100 pc (Bloeman 1987). So a direction with substantial X-ray emission will extend nearly to the top of the neutral hydrogen disk, and the amount of neutral hydrogen in that direction will be substantially lower.

Fitting the data with the only free parameter in this model, the pressure in the bubble, leads to a pressure P/k of 7100 – 9000 K cm^{-3}(Snowden *et al.* 1990). Snowden *et al.* (1990) calculated the parameters for two models of this type, one where the cavity was formed by "removing" material, and another where the material was "swept out." I extract some pertinent numbers from their paper in Table 1.1.

The pressure of the local bubble in this model can be independently estimated from the B and C band emission, since the gas is assumed to be uniform within the bubble. We can calculate $K_{eq}(T)$, the band count rate per emission measure by integrating the spectrum of an equilibrium plasma convolved with the B or C band response curve. Then the count rate in the given band is just

$$I_{\text{counts/sec}} = K_{eq}(T) n_e^2 d \tag{1.2}$$

where n_e is the electron density, and d is the distance to the bubble edge. For the B band, $K_{eq}(10^6 K) = 1.60 \times 10^4$ cts s^{-1}/(cm^{-6} pc), and for the C band $K_{eq}(10^6 K) = 3.95 \times 10^4$ cts s^{-1}/(cm^{-6} pc) (McCammon *et al.* 1983). Assuming a bubble radius of 100 pc, then, we can use the observed all-sky average rates (B band 49 cts/s and C band 125 cts/s) to get $n_e \approx 0.0055$ cm^{-3}, and therefore a thermal pressure of $P/k = 2 n_e T \approx 11,000$ K cm^{-3}. This is not equal to the model pressure due to changes in the plasma emission codes (and thus K_{eq}) used in McCammon *et al.* (1983) and in Snowden *et al.* (1990).

While successful, this model is phenomenological; it reproduces the data without explaining why or how this situation was reached.

1.2.3 Local Bubble

It is clear that the creation of such a large cavity must have been an extremely energetic event or process. The energy in the local bubble in the displacement model matches that of an supernova explosion, suggestive evidence that the local bubble is an old supernova remnant. Detailed models of this hypothesis have not been successful, though. The most detailed effort in this direction to

date was by Edgar & Cox (1993) who used a one-dimensional hydrodynamical code with detailed ionic evolution to generate the x-ray spectrum from a supernova remnant as it evolves in time. They showed that while the size of the local bubble can be matched, and the spectrum can be matched, to fit both simultaneously required both a huge explosion (5×10^{51} ergs, 5-10 times that of a normal supernova) and a very high external pressure.

Edgar & Cox suggested two additions to their model, adding dust and using multiple explosions instead of a single large explosion. These suggestions are explored later in this dissertation.

1.2.4 Other models

Interstellar gas heated to $10^6 - 10^7$K will cool primarily via collisional excitation of atoms; bremstrahhlung radiation is small until T $> 10^7$K. However, by a quirk of atomic physics and cosmic abundances, there is a dearth of easily-excited collisional lines in ions in this temperature range. Thus, gas at this temperature will cool slowly, taking $\sim 10^5/n_e$ years to cool from 10^6K to 10^4K. (Cox & Anderson (1982); Smith *et al.* (1996)) Cox & Smith (1974), combining the slow cooling time of hot gas with the known supernova rate and models of their size discovered that the Galaxy might contain pervasive tunnels of hot gas. This idea was then expanded upon by McKee & Ostriker (1977) who found that the Galaxy should consist largely of hot gas at $\sim 3 \times 10^5$K; but since this is not hot enough to create the SXRB, their model also required a recent nearby supernova to heat the local ISM.

Breitschwerdt & Schmutzler (1994) have put forth a model where the local

bubble is actually a cool superbubble, the remnant of ~ 10 supernova explosions with the most recent explosion 4×10^6 years ago. The bubble has a temperature $T \approx 6 \times 10^4$K, having cooled both adiabatically and radiatively, but is still over-ionized and far from equilibrium. The x-ray emission results from recombination radiation, as the medium slowly returns to equilibrium. The electron density predicted is $\approx 0.024\text{cm}^{-3}$, and the pressure, $nT \approx 2600$ K cm^{-3}, is much lower than the displacement model predictions. This may not be enough to support the bubble against the weight of the halo (Cox & Snowden 1986). New observations with high spectral resolution, made with DXS and subsequent instruments, may be able to discriminate between a hot bubble and a cold recombining one.

1.3 Conclusions

There is a certain irony in our difficulty in understanding the soft X-ray background. The observations show that this background is nearly uniform at the lowest wavelengths, where absorption should be most dramatic. Basic physics tells us that the source must be nearby, at least in high density regions such as the plane of the galaxy. So we have a union of the observational and theoretical preferences, a region well defined in space and wavelength, nearly isotropic in emission. And yet this is, paradoxically, the most difficult scenario to understand. In chapter 3 this question will be further addressed, using multiple supernova remnants widely spaced in time to model the observations.

Chapter 2

A Simplified Model of Time-Dependent Cooling and Grain Destruction in Hot Dusty Plasmas

2.1 Introduction

Most models of cooling of hot interstellar plasmas have avoided the complications of the possible dust content of the gas, making the hopeful assumption that dust will be short-lived in such a hostile environment. That assumption, however, is rarely valid. Dust can be present for long periods of time, can cause modest changes in the evolution of hot gas and appreciably alter its observable characteristics. There have been many explorations of these important aspects of the dust/hot gas interaction, beginning perhaps with Ostriker and Silk (1973) who showed the importance of the dust cooling coefficient in high temperature gas. Examples of those who have explored both the cooling rate and dust sputtering include Burke and Silk (1974), Draine and Salpeter (1979), and McKee *et al.* (1987). Itoh (1989) explored the effect of dust sputtering on the ionization structure of x-ray emission of very high temperature

shocks. Dwek (1981) considered the cooling and evolution of supernovae remnants (SNR) during the Sedov phase, and Vancura *et al.* (1994) explored in considerable detail the structure of steady state adiabatic shock waves.

The most important results of this effort have been that dust survives the shock transition, passing into the hot post-shock environment, and that its radiation there is important and has been seen at the expected rate. Also important is that at temperatures below a few million Kelvins, dust is destroyed gradually over a very protracted period (owing to the broad distribution of grain sizes), and that except at rather low temperatures and in slow shocks the destruction takes place via thermal sputtering.

In this paper we describe the elementary approach we have taken toward incorporating these obviously important effects into hydrodynamic calculations of phenomena involving hot gas. Because of this focus we are able to make several simplifications. We are interested in dynamics and, in particular, gas which remains hot long after it is initially heated. We are not exploring the intimate details of any aspect of radiative shocks beyond the fact that the gas cools, or the distressing problem that dust destruction estimates significantly exceed those for its formation. As a result, we include only thermal sputtering by ions as a destruction mechanism, and assume that on average, grains and gas are comoving coupled fluids. The recent paper by Vancura *et al.* (1994) provides an excellent example and reference set for the more complete description.

The resulting codes should be very useful for studying ancient hot gas bubbles as a possible model for the Local Bubble, fountains of hot gas rising out of

the galactic plane (or winds from the galactic center), the hot interiors of individual old SNR bubbles in the galactic plane and halo, models of superbubble evolution (for which much of the hot gas may have been heated by transport processes rather than by shocks), and many other large scale phenomena.

The basic information required for this project includes:

- total elemental abundances
- fraction of each element found in grains in a diffuse interstellar environment
- distributions of those elements among grain types
- grain size distributions
- mean grain densities (or porosity of grains)
- chemical inhomogeneities of the grains
- rates of thermal sputtering by nuclei
- rate of energy deposition in the grains due to electron impacts

We discuss our assumptions about each of these and the reasons for ignoring other effects in section 2. In section 3 we present the method for incorporating this dust model into a code which calculates gas cooling rates. Finally, in section 4 we present representative single parcel evolutions (isothermal and isobaric) which follow the evolution of dust mass, cooling rate, and for the latter two, temperature. These results are very valuable in evaluating the importance of including dust in models of specific systems in which hot gas plays an important role.

As a final example, we present the effect that inclusion of dust has on the column densities of C IV, N V, O VI, Si IV, S IV and S VI in one-dimensional isochoric and isobaric cooling flows, such as might exist in a galactic fountain. These results can be compared with Edgar & Chevalier's (1986) results calculated in a similar model without dust.

2.2 Dust Properties

Consultation with John Mathis (1994, private communication) prompted us to include only the two most refractory components of interstellar dust, referred to as silicate grains and small carbon grains. We neglect grain mantles which are not expected to be present in very diffuse interstellar conditions, and polycyclic aromatic hydrocarbons, which can easily be destroyed in the hot plasmas under consideration.

Our choices for the quantities of the various elements found initially in the gas phase, in the silicate dust, and in the carbon particles are shown in Table 2.1, both in the common logarithmic notation and in parts per million relative to hydrogen. The total abundances are taken from Anders & Grevesse (1989) and the depletions from John Mathis (1992, private communication) and Spitzer & Jenkins (1975). In addition, we assume that the silicate dust consists of a homogeneous mixture of the elements within it.

The structure of silicate dust grains is not well known; recent evidence from cometary studies and x-ray halos around stars suggests that the mean internal density of the dust grains might be quite low and thus the grains are fluffy or porous. (Smirnov *et al.* , 1988 and Mathis *et al.* , 1994) However, there is no

conclusive evidence in either direction, so all results were calculated for both a solid, dense grain, and a fluffy one five times less dense. We will occasionally refer to these by their respective porosities, or empty volume fractions of 0 and 0.8, respectively. We use the following size distributions for silicate grains:

$$\frac{dN}{da} = Aa^{-p} \quad \text{for} \quad a_1 < a < a_2 \tag{2.1}$$

where a is the grain radius. For the dense grains, $a_1 = 0.03$ μm, $a_2 = 0.23$ μm and $p = 3.5$, and for the fluffy grains, $a_1 = 0.03$ μm, $a_2 = 0.90$ μm and $p = 3.5$. This is the distribution given in Mathis & Whiffen (1987) with one modification, changing from $p = 3.7$ to $p = 3.5$ for silicates, for reasons given later.

The mass in silicate or carbon grains per hydrogen atom is thus given by

$$M_g = \overline{\rho_g} \int_{a_1}^{a_2} \frac{4}{3}\pi a^3 \frac{dN}{da} da \tag{2.2}$$

The normalization constant was chosen such that the elemental abundances yield the chosen mean density for the grains. For the silicates, we have taken the density of solid grains to be $\overline{\rho}_g = 2.65$ g cm^{-3}, and porous grains to be $\overline{\rho}_g = 0.53$ g cm^{-3}.

For carbon grains, much less is known about the detailed size distribution, especially for small grain sizes. We used the distribution from Mathis, Rumpl, and Nordsieck, with p = 3.5, $a_1 = 0.005$ μm, $a_2 = 1.0$ μm, and $\overline{\rho} = 2.0$g cm^{-3}.

With the above choices, and the elemental abundances of Table 2.1, we get the results shown in Table 2.2: grain size proportionality constant A, number per H atom, and mass per H atom.

The sputtering of both silicates and small carbon grains by impacts with

nuclei have been studied theoretically. We use the rates of Tielens *et al.* , 1994. The rates are quoted as polynomial fits to the function $\dot{a}(T)$, where $\dot{a} = da/dt$. In the case of silicate grains, the calculations corresponded to a mean grain density of 2.65 g cm^{-3}. For the fluffy grains, we have assumed that the sputtering of individual atoms is unaffected by the difference in porosity, making $\dot{a}$ inversely proportional to grain density.

At the temperature range of interest in this paper, cooling from dust grains arises primarily from deposition of energy by electron collisions with grains, and subsequent radiation in the infrared. The basic principle is that $nv/4$ impacts occur per unit area per second, bringing energy $m_e v^2/2$, for a total cooling rate per unit volume

$$\epsilon \sim n_e(\frac{m_e < v^3 >}{8})(S/n_H)(n_H) \tag{2.3}$$

where S/n_H is the grain surface area per hydrogen atom, given in our case by

$$S/n_H = \int_{a_1}^{a_2} 4\pi a^2 \frac{dN}{da} da. \tag{2.4}$$

We have ignored the effects of grain charging, because the grain charge is thought be be negligible at temperatures above $\sim 2 \times 10^5$K. (McKee *et al.* , 1987). Between 10^4K and 2×10^5K, the cross section for interactions with electrons would be considerably reduced by charges on the grains, which would significantly reduce dust cooling. However, the cooling due to dust is unimportant compared to that of the gas at such temperatures.

For constant grain properties, these considerations then give rise to a cooling coefficient

$$L_{dust} = \frac{\epsilon}{n_e n_H} \sim C T^{3/2}. \tag{2.5}$$

Early evaluations (*e.g.* Ostriker & Silk, 1973) indicated that this cooling could exceed normal gas cooling for $T \geq 10^6 K$.

This simple picture, however, leads to serious overestimates of dust cooling. The most important additional requirements on a model are:

- using reduced grain surface area after some sputtering has occurred,
- taking into account the complete penetration of high speed electrons through very small grains, with a subsequent reduction in the energy deposition.

The first effect, the reduction of all grain surface areas and disappearance of the initially smaller grains requires only that size reduction be incorporated into the surface area integration. The second effect depends in detail upon the grain size and type and the electron energy. This was extensively studied in Dwek (1987), and Figures 3a,b of that paper present graphs of $h_e(a,T)$, the fractional efficiency in energy deposition due to electron penetration of the grains. We fit the curves by an approximate formula:

$$h_e(a,T) = \frac{0.875a}{a+\beta(T)} \tag{2.6}$$

where $\beta(T) = 0.01(T/T_c)^{1.75}(\rho_{solid}/\rho)$ μm, with $T_c = 3.8 \times 10^6$K for graphite dust and $T_c = 6 \times 10^6$K for silicate dust. While not perfect, this formula fits the data well in general, overestimating the cooling for small grains and underestimating it for large grains. It is good to within 75% everywhere of interest, is usually much better, and has the advantage of being easily calculated.

Thus, our formula for the cooling coefficient due to dust is

$$L_{dust} = \frac{4\sqrt{2\pi}(kT)^{3/2}}{{m_e}^{1/2}} \sum_i A_i \int_{max(a_1-\delta,0)}^{a_2-\delta} \frac{a^2}{(a+\delta)^p} \frac{0.875\,a}{a+\beta(T)} da \tag{2.7}$$

where a is a grain's current radius, $a+\delta$ is its radius before sputtering has reduced each grain radius by $\delta = \int_{t_0}^{t} [-\dot{a}/n] n dt$, and the sum is over the two types of grains. The coefficient in front is from the factor $m_e < v^3 > /8$ in ϵ. In the general case with arbitrary p, this reduces to a hypergeometric function which is not convenient to evaluate except via tables. However, in the special case where p is integer or half-integer, the integral can be solved analytically in a form easy to compute. In the case where $p = 3.5$, we get:

$$\int \frac{a^3 da}{(a+\delta)^{7/2}(a+\beta)} = \frac{2\delta a^2(3-3\beta\delta+\delta^2)}{(\beta-\delta)^3(a+\delta)^{5/2}} \tag{2.8}$$

$$+\frac{2\delta a(15\beta^2\delta - 13\beta\delta^2 + 20\delta^3)}{3(\beta-\delta)^3(a+\delta)^{5/2}} \tag{2.9}$$

$$+\frac{2\delta(33\beta^2\delta^2 - 26\beta\delta^3 + 8\delta^4)}{15(\beta-\delta)^3(a+\delta)^{5/2}} + K(a,\beta,\delta) \tag{2.10}$$

where $K(a,\beta,\delta)$ depends upon the value of $\beta - \delta$:

$$K(a,\beta,\delta) = \frac{2\beta^3}{(\beta-\delta)^{7/2}} \mathrm{ArcTan}\Big(\sqrt{\frac{a+\delta}{\beta-\delta}}\Big) \quad \text{for} \quad \beta-\delta > 0 \tag{2.11}$$

$$K(a,\beta,\delta) = \frac{2\beta^3}{(\delta-\beta)^{7/2}} \mathrm{ArcTanh}\Big(\sqrt{\frac{a+\delta}{\delta-\beta}}\Big) \quad \text{for} \quad \beta-\delta < 0 \tag{2.12}$$

However, in the special case where $0.95\,\delta < \beta < \delta$ the above solution is numerically problematic. In this case, it is possible to do an expansion on the small term $\gamma = \delta - \beta$, resulting in the expression

$$\int \frac{a^3 da}{(a+\delta)^{7/2}(a+\delta-\gamma)} = \int \frac{a^3 da}{(a+\delta)^{9/2}} + \gamma \int \frac{a^3 da}{(a+\delta)^{11/2}} \tag{2.13}$$

To check the final result, in Figure 2.1 we show the equilibrium gas and initial dust dust cooling coefficients versus temperature. The calculated dust cooling is compared with the result given in Dwek (1987). Gas cooling is shown for the Raymond & Smith (1977, 1993) code, both for depleted and

solar abundances. In agreement with Ostriker & Silk (1973), Figure 2.1 shows that the cooling of pristine dust is much larger than the equilibrium gas cooling for high temperatures. As we shall see, however, this comparison can be quite misleading.

2.3 Use with Gas Evolution Programs

A common example of the use of gas evolution codes is in connection with a hydrodynamic simulation with a Lagrangian mesh, following the evolution of the location and state of a set of interacting gas parcels. The hydrodynamic code evaluates velocities, locations, densities, and temperatures, but requires the cooling coefficients for the gas parcels at each time step. The gas code uses ionization, recombination, and excitation rates to follow ion concentration evolution and to provide the cooling coefficients. It is accessed separately for each parcel at each time step, with the current ion concentrations, density, and temperature. It returns the new ion concentrations and the present gas cooling coefficient.

When a dust code is grafted into this arrangement, the gas phase abundances become variables. In addition, one must store for each parcel two more variables describing the current state of grain destruction (one for each grain type). Thus, the grain code is accessed for each parcel with the current gas phase abundances, ion concentrations, two grain destruction parameters, density, temperature, and time step. It calculates the mass returned to the gas during the time step, the new gas phase abundances, renormalized ion concentrations (assuming freshly sputtered material is neutral), and the grain

cooling coefficient. The main program then sums the gas and grain cooling coefficients and continues. In models which decouple the gas and grain motions (*e.g.* Vancura *et al.* (1994)) much more elaborate bookkeeping is required.

When snapshots of the structure are desired, one must save for each parcel the current gas phase elemental abundances in addition to the usual ion concentrations, density, temperature, location, velocity, and so on to be able to compute ion density distributions, column densities, line profiles, and emission spectra.

2.4 Single Parcel Evolutions

2.4.1 Isothermal Evolution

Starting with a parcel of gas at equilibrium ion concentrations appropriate to $T_0 = 2 \times 10^4 K$ (so that hydrogen is fully ionized), we raise the temperature suddenly to a constant high value T_h. The gas scrambles upward in ionization, the gas cooling coefficient drops rapidly as the lower stage ions disappear, and the dust gradually sputters, lowering the dust cooling coefficient but raising the gas phase abundances.

For single parcel evolutions, the heating, cooling, ionization and recombination rates are all proportional to the electron density n_e. As a consequence, evolution depends only on the composite variable fluence:

$$f \equiv \int n_e dt. \tag{2.14}$$

Figure 2.2 shows the contours of dust mass fraction remaining as a function of fluence and T_h for dense silicate dust; graphite is not included due to its

small mass contribution. One of the principal features of this result is that dust sputtering on the assumed grain size distribution is a very protracted process. It demonstrates, for example, that at a temperature of 10^6 K and electron density of 5×10^{-3} cm^{-3} (parameters typical in Local Bubble models), complete sputtering of dense silicate dust takes $\sim 3 \times 10^8$ years, far longer than any age estimate for the Local Bubble, while dust is 10% and 50% sputtered at 3×10^6 and 2×10^7 years respectively. At a given grain size our fluffy dust (Figure 2.3) is sputtered five times faster, but because the maximum grain size is 3.9 times larger, total destruction is only about 20% earlier.

Figure 2.4 shows the evolution of the cooling coefficient and dust mass with fluence, for gas with graphite and dense silicate grains initially shocked from $T_0 = 2 \times 10^4$ to $T_h = 10^6$ K and then held at that temperature. Figure 2.5 is the same but for fluffy silicate grains. The cooling from gas (principally line emission) and from dust are shown along with the total. The dust mass evolution again illustrates the length of the sputtering process. The cooling graphs show that dust is an important coolant before the numerous tiny grains are destroyed. Note that there remains a significant amount of dust mass present long after its cooling contribution has become negligible.

2.4.2 Isobaric Evolutions

In our isobaric (constant pressure) conditions, gas is suddenly heated from equilibrium ionization at $T_0 = 2 \times 10^4 K$ and then allowed to cool according to

$$\frac{dT}{df} = \frac{1}{n_e}\frac{dT}{dt} = -\frac{2}{5}\frac{L}{\chi k_B}\frac{1}{1.1} \tag{2.15}$$

where $Ln_e n_H = Ln_e n/1.1$ is the volume emissivity, $p = \chi n k_B T$ is the pressure, $\chi = (n + n_e)/n$ is the number of free particles per nucleus, and k_B is the Boltzmann constant. (We have assumed $n = n_H + n_{He} = 1.1 n_H$, which for fully ionized gas yields $\chi = 2.3/1.1$.)

With these conditions, the cooling coefficient is initially large due to the presence of neutrals and low stage ions, but decreases rapidly as they ionize to higher stages. If T_h is very high, dust cooling is important after the initial "ion flash," but as the temperature drops, ion cooling again becomes dominant. Dust sputtering returns mass to the gas phase, but unless the initial temperature was above a critical value, sputtering is incomplete.

Figure 2.6 shows the isobaric evolution of the cooling coefficient and temperature for $T_h = 10^6 K$, comparing runs with and without dust (the latter starting with all material in the gas phase), for both silicate porosities.

Figure 2.7 shows the value of the fluence, f_{cool}, at which the temperature drops to $10^4 K$, for isobaric runs, with and without dust. Also shown is the fluence at which the dense and fluffy dust grains are completely sputtered in isothermal evolutions.

Figure 2.8 shows the dust mass fraction remaining in the gas when it finishes cooling, as a function of temperature T_h, for isobaric runs with both fluffy and dense grains.

Figures 2.9 and 2.10 show evolution of the cooling coefficient with temperature for runs beginning at $T_h = 10^6$K and 10^7K. Results are shown for isobaric evolutions without dust and with dust of each grain type.

Figure 2.11 shows one spectral consequence of (dense) dust sputtering by comparing the strengths of two emission lines in the soft x-ray regime. For gas

with unsputtered dust, *i.e.* with depleted abundances, the S VIII 63.5 Å line dominates the 1/4-KeV x-ray emission spectrum. However, for $f \gtrsim 10^5 \mathrm{cm}^{-3}\mathrm{yr}$, Si VIII 61.03 Å is stronger. Thus the degree of sputtering in hot gas can potentially be measured by observing the soft x-ray spectrum.

2.5 Fountain Column Densities

We extended the calculations of Edgar & Chevalier (1986) to include the effects of dust depleting the available ions in a cooling fountain with an initial temperature of 10^6K. We present in Table 2.3 the column densities of some astrophysically important ions which can be observed in the ultraviolet: C IV, N V, O VI, Si IV, S IV, and S IV. Four different models were considered: isobaric, isochoric, and two "transition" models that begin isobaric and switch to isochoric at either $T_{tr} = 2.2 \times 10^5$ K or $T_{tr} = 4.7 \times 10^5$ K. These same cases were considered by Edgar & Chevalier. There are some differences between our dust free results in Table 2.3 and those of Edgar & Chevalier, mostly due to different choices of solar abundances. When using the same abundances, we get good agreement.

For an initial temperature of 10^6K, dust destruction is incomplete in the fountain, lowering the column densities of carbon and silicon ions. Because the cooling of the gas is slightly slower with these depletions, the column densities of less depleted elements' ions are slightly enhanced.

2.6 Discussion

From the results presented in Figures 2-11, a number of general conclusions can be drawn. From Figures 2.2 and 2.3, one finds that the timescale for complete sputtering of dust is long compared to other timescales of interest, even for fluffy dust. Between $T = 0.3$ and 40×10^6K, at a typical interstellar pressure of $p/k = 10^4$ cm^{-3}K, the complete sputtering timescale is approximately constant at 2.5×10^8 yr (within a factor of 2). It is even longer for lower or higher temperatures. As we pointed out previously, this is much longer than most estimates of the age of the Local Bubble. In the diffuse hot portions of the Cygnus Loop, the pressure is a factor of 100 higher. The corresponding sputtering time is only 3×10^6 yr, but even that is about a factor of 200 longer than the age of the remnant. Infrared emission from hot dust behind the adiabatic (x-ray emitting) shocks has been found and shown to be consistent with the dust survival predicted by models similar to ours. (Arendt *et al.* , 1992)

Such numbers must be considered cautiously, however. From Figures 2.2, 2.3, 2.4, and 2.5 it is clear that essentially all of the dust mass has been returned to the gas long before the largest grains are completely gone. For a heavily depleted element such as iron, even a few percent of mass return has a very large effect on the gas phase abundance and spectrum. In the Local Bubble (age 10^5 to perhaps 10^7 yr), a non-negligible amount of sputtering may have occurred.

From Figures 2.7 and 2.8, we find that at $T \gtrsim 4 \times 10^6$K, complete dust sputtering occurs prior to substantial radiative cooling of the gas. We conclude that, for those temperatures at which pristine dust would dominate the

total cooling rate, it cannot survive long enough for its radiation to alter the thermal history very much. Conversely, for temperatures between 10^4K and 3×10^5K, both thermal dust sputtering and dust cooling are small. So if thermal sputtering is the only important destruction mechanism, gas in this temperature range will evolve with fixed (but depleted) elemental abundances, and be dominated by gaseous processes.

Again, these conclusions must be considered with caveats. Quite often, very high temperature gas cools at a much higher rate than that determined by its radiative emissivity, through adiabatic expansion (for example in the Sedov blast wave), or via thermal conduction to cooler material, or both. As a consequence, such gas will often not complete its sputtering before reaching lower temperatures at which the grains can survive (see also Dwek, 1981). During this evolution, the grains can provide a large fraction of the emission, though they do not radiate a significant fraction of the total energy available. Similarly, gas below 3×10^5K has often been much hotter in the past and can have had a significant amount of dust sputtering. Clearly, the history of a gas parcel must be considered carefully when an estimate is made of its dust content or gaseous abundances (Dwek, 1981).

Many aspects of the cooling behavior of shock heated material are evident in Figures 2.4 through 2.6. At 10^6K with fluffy (dense) dust, the initial dust cooling coefficient is somewhat higher (lower) than the equilibrium gas cooling coefficient; however, at early times, cooling is dominated by the gas in a brief "ion flash." The latter is due to the initial presence of low stages of ionization radiating profusely in the hot gas. As the ionization level scrambles upward towards equilibrium, the flash dies out, in this case after a fluence of about 1000

$cm^{-3}yr$. For a time thereafter, dust is an important coolant. It decreases due to sputtering at fluences $\gtrsim 3 \times 10^4$ $cm^{-3}yr$. The evolutions of isothermal and isobaric cases are nearly identical for fluence less than about 3×10^4 $cm^{-3}yr$, as the total temperature change is quite small. Finally the isobaric case begins to cool significantly, showing a sharp peak in the cooling coefficient as it passes through temperatures at which the cooling function is large (see Figures 2.6, 2.9, and 2.10). The isothermal case has a gradually increasing gaseous cooling coefficient as continued sputtering completes the mass return. Its final plateau is the equilibrium cooling coefficient at 10^6K for undepleted abundances.

The temperature of 10^6K is in the most complex regime, where cooling and dust sputtering have similar timescales, and (coincidentally) grain and gas cooling coefficients are similar in magnitude. During its history the gas experiences radically different cooling coefficients. The gas and grain cooling contributions are so similar that in Figure 2.6 the total cooling rate curves for the two dust types straddle the curve for the dust free evolution.

Despite this, some simplifying approximations to the cooling coefficient are possible, as the nearly straight lines of the cooling fluences in Figure 2.7 suggest. Supposing for the moment that the cooling coefficient at each temperature were a well-defined function, L(T), the cooling fluence for isobaric evolution would be

$$f_{cool}(T_h) = \frac{5}{2}\chi k_B \int_{T_0}^{T_h} \frac{dT}{L(T)} \tag{2.16}$$

while for isochoric evolution the 5/2 is replaced by 3/2. Apart from very minor wiggles (due to real features in the cooling curve), the cooling fluences in Figure 2.7 are well fit by a $T^{3/2}$ proportionality. Such a relationship has long been used to approximate the cooling; it is originally due to Kahn (1975,

1976), and the corresponding cooling coefficient, $L(T) \approx \alpha T^{-1/2}$ is called the Kahn approximation. The effective value of α generally used is 1.3×10^{-19} cgs (e.g. Cui and Cox, 1992, and references therein), but 1.0×10^{-19} cgs is a better fit to the cooling fluences in Figure 2.7 and the cooling function itself (Figures 2.9 and 2.10) for $T > 4 \times 10^5$K.

The Kahn approximation has the useful feature that the cooling timescale from initial conditions T_h, n_h

$$t_{Kahn}(T_h, n_h) = \frac{\chi k_B}{\alpha n_h} T_h^{3/2} = 0.9 \times 10^5 \text{ yr } \left[\frac{T_h}{10^6\text{K}}\right]^{3/2} \left[\frac{\text{cm}^{-3}}{n_h}\right] \qquad (2.17)$$

is independent of the subsequent thermal and pressure history of the gas. The fact that this relationship is apparently reliable over the entire range of T_h from 3×10^5 to 10^8K, independent of the initial dust content of the gas will be extremely useful for approximate modeling.

Figures 2.9 and 2.10 show the time-dependent cooling coefficient versus the time-dependent temperature, for cases with and without dust and for $T_h = 10^6$ and 10^7K. Several features are noteworthy. Both the relative sizes of the ion flash and the duration of the dust destruction epoch are very short at $T_h = 10^7$K, but in the $T_h = 10^6$K case the dust is never fully destroyed. At lower temperatures, the dust contribution to cooling is negligible, so with dust the $T_h = 10^6$K cooling curve is lower than the other cases, due to its depleted abundances.

If the eight curves of Figures 2.9 and 2.10 are superimposed (rather than 2 sets of four as shown), one finds that the post flash evolutions are nearly identical. There is little dependence on initial dust content of the gas (solid versus dotted), or on initial temperature. The latter effect was previously noted by Edgar and Chevalier (1986). The differences between the various

curves below 10^6 K is due almost solely to the different gas phase abundances. In the fluffy grains, $T_h = 10^7$K case, nearly all the dust is returned to the gas phase well before the temperature reaches 10^6K. However, in the dense grains, $T_h = 10^6$K run, there is a pronounced dip in the cooling curve, due to the dust which is no longer cooling effectively by itself but is still locking up important coolants.

Finally, Figure 2.11 shows an example of the sensitivity of the spectrum of hot gas to the effects of non-equilibrium ionization and dust content. The model starts with gas and dust at $T = 2 \times 10^4 K$ and then jumps to $T = 10^6 K$, after which the system is isothermal. At 10^6K, both the 61.0Å line of Si VIII and the 63.5Å line of S VIII are important emitters. The figure shows how the strengths of these two lines vary with fluence, while the temperature is held constant. Initially, the gas is singly ionized, but after a fluence of about 6500 cm^{-3}yr, the relevant ion populations approach equilibrium. In our model, none of the sulfur is in the dust, but at first 97% of the silicon is. The rise and then small decrease in the sulfur line strength is due to the scrambling of the gas through the S VIII ionization state, until it reaches equilibrium. During the subsequent period (fluence $\gtrsim 3 \times 10^4$ cm^{-3}yr), the silicon line strength increases dramatically, as silicon returns to the gas phase.

The above results offer a method of approximate dating of hot gas with good x-ray spectral information, though it must generally be applied within the context of a specific model. The age of hot gas, *i.e.* the time since heating, can be inferred from the dust sensitive spectral features, given separate information on the density and temperature structures and a scenario for the past history. In addition, because of the uncertainties of dust properties, this sputtering

date will not be absolutely calibrated. Still, it will be an extremely useful tool in helping to select among models for the approximately useful subset.

We have suggested that inclusion of dust evolution and cooling in hydrocodes has both a small effect on the thermal evolution and large effects on observables. We can give a better idea of the importance to the thermal evolution. In our isobaric evolutions with $T_h \gtrsim 10^6$K, the total energy radiated by dust during the entire cooling evolution was approximately 100 eV $(T_h/10^6K)^{1/2}$ per hydrogen atom, out of a total enthalpy of 500 eV $(T_h/10^6K)$.

The fraction of energy radiated by dust peaks in the vicinity of 10^6K, at about 20%, droppping sharply at lower temperatures. Thus these losses are never as significant as the uncertainties in the gas cooling coefficient itself. Nevertheless, some caution is required in their interpretation. For example, in a Sedov SNR evolution, the energy is effectively reused to heat more and more gas to ever lower temperatures. It is easily possible that as much as 30% of the total explosion energy is radiated by dust prior to the shell formation epoch (see Dwek, 1981).

The authors acknowledge useful discussions with John Mathis and Eli Dwek. This work was supported by NASA grants NAGW-2532 and NAG5-629, and one of the authors (RKS) is supported on NSF and WARF Fellowships. LGK acknowledges support from an Undergraduate Hilldale Fellowship from the University of Wisconsin–Madison.

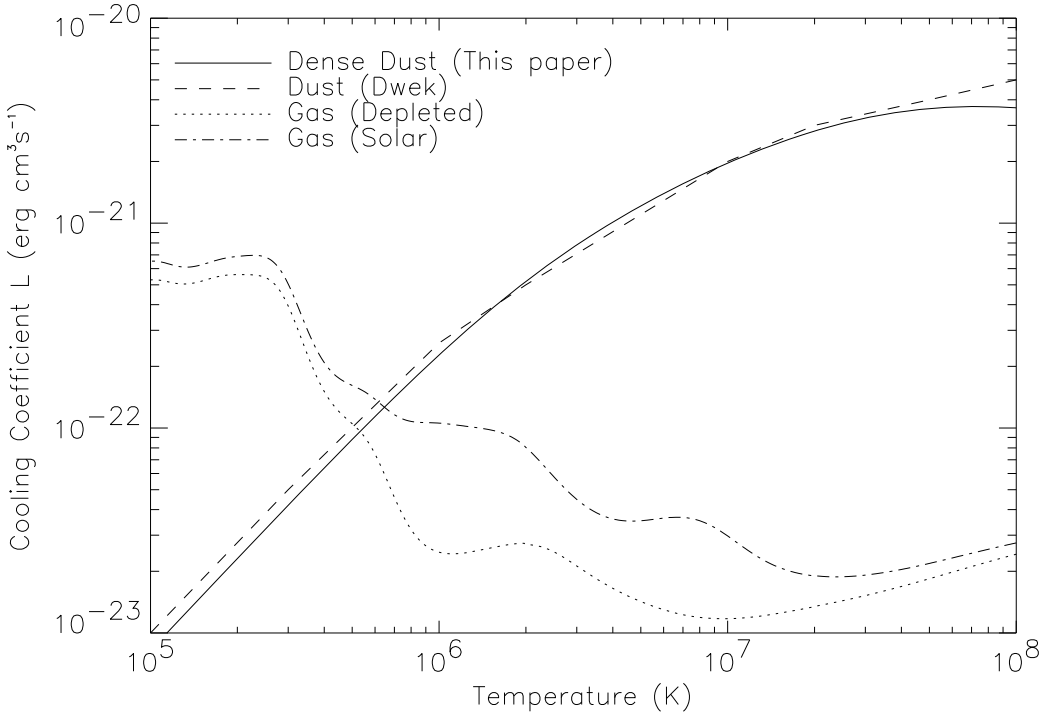

Figure 2.1: Collisional Equilibrium Gas and Initial (Dense) Dust Cooling coefficients vs Temperature

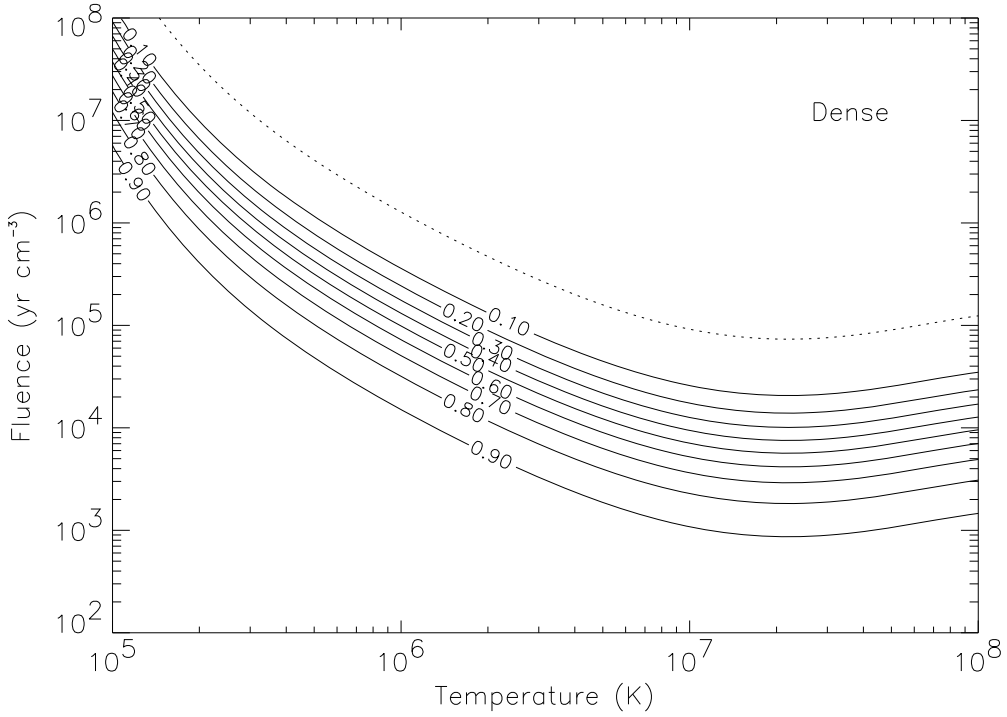

Figure 2.2: Dense silicate dust mass fraction remaining versus fluence in an isothermal evolution versus temperature, dotted line indicates completion of dust sputtering.

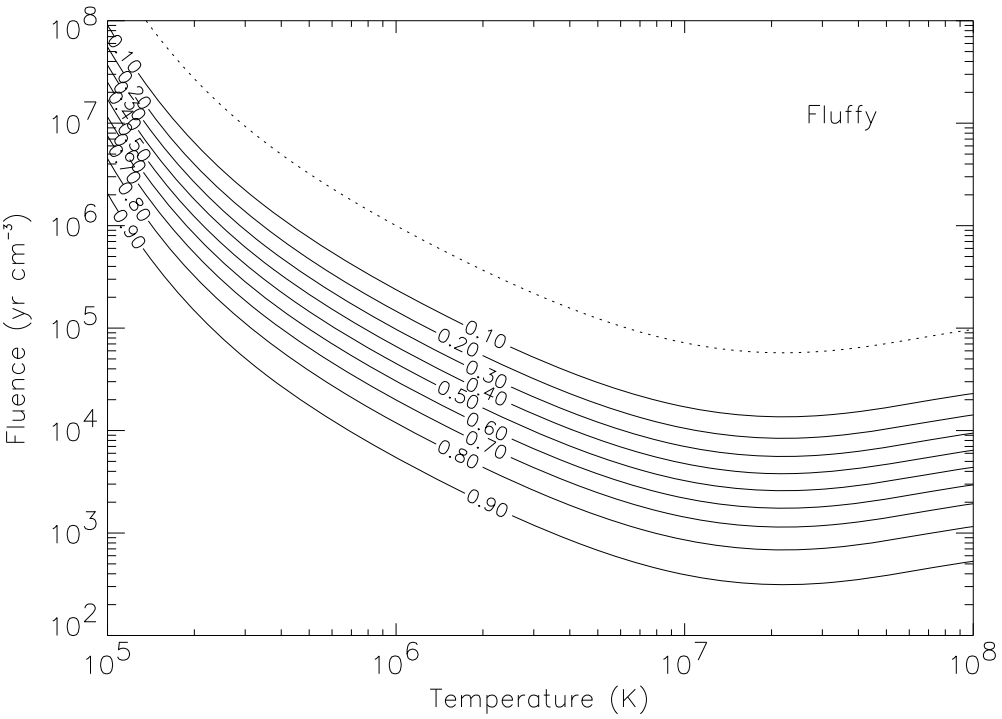

Figure 2.3: Same as Figure 2 for fluffy dust.

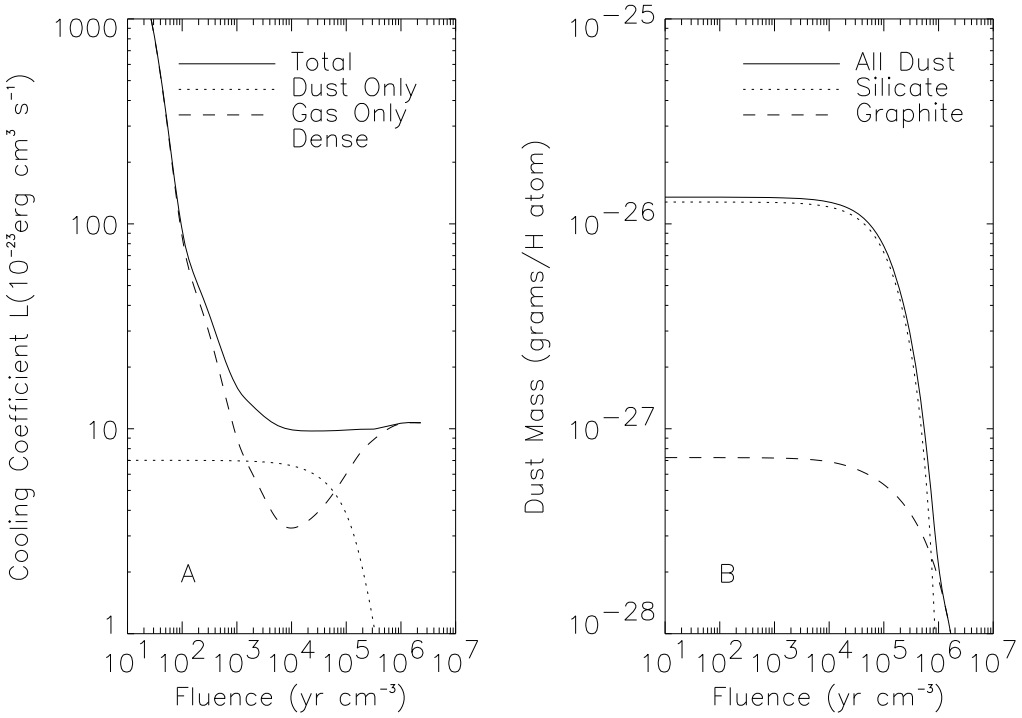

Figure 2.4: Evolution of cooling coefficient (a) and dust mass (b) for isothermal model at 10^6K with dense dust. Initial condition was ionization equilibrium at 2×10^4K.

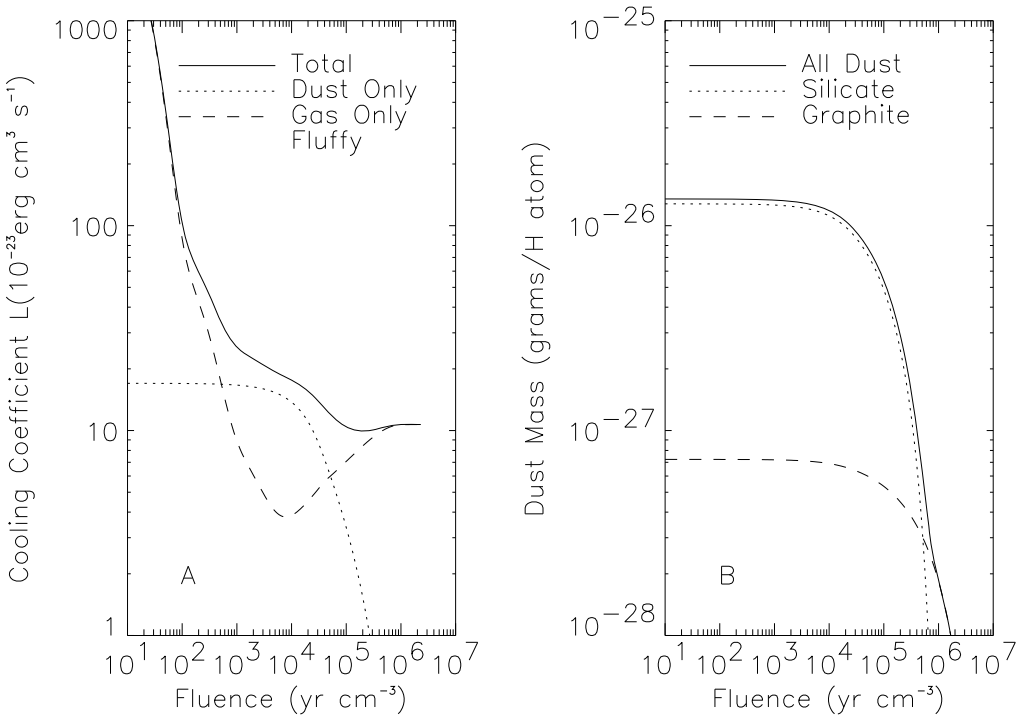

Figure 2.5: Same as Figure 4 for fluffy dust.

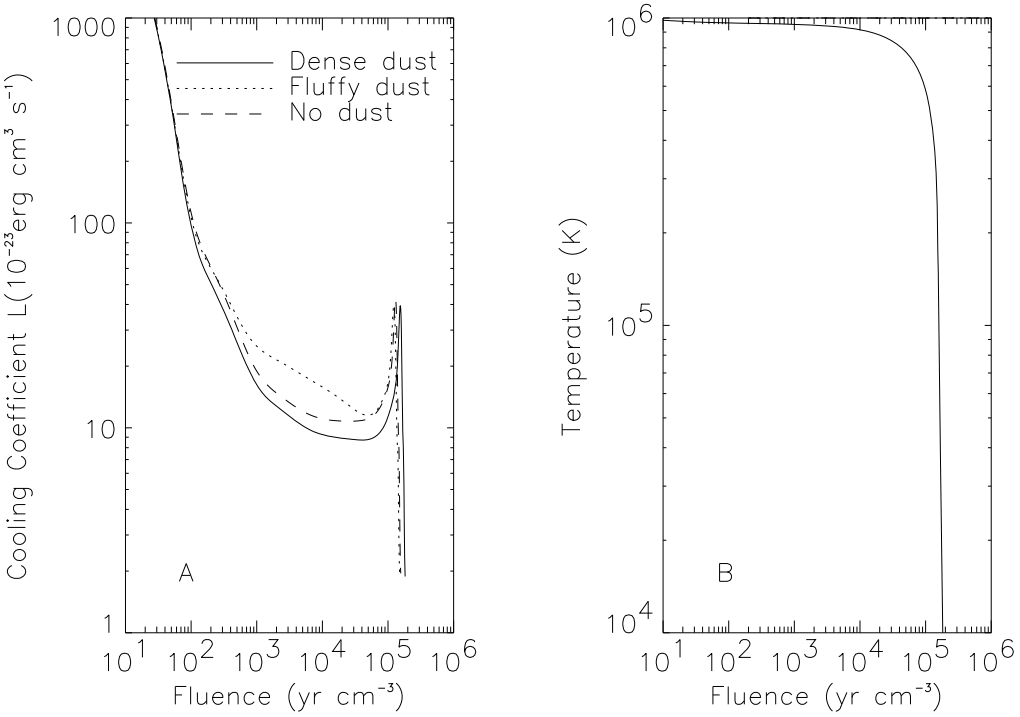

Figure 2.6: Evolution of cooling coefficient (a) and temperature (b) for isobaric models. Initial condition was ionization equilibrium at 2×10^4K and kinetic temperature of 10^6K.

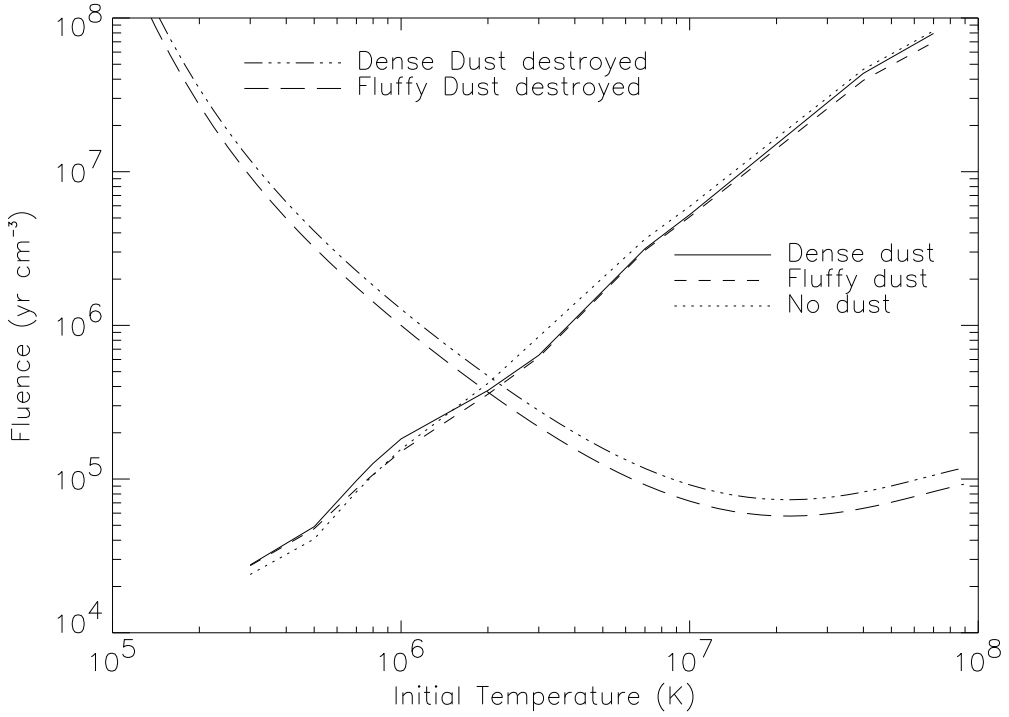

Figure 2.7: Fluence required in isobaric evolution to cool to 10^4K, as a function of initial temperature. Also shown are the fluences at which dust would be fully destroyed in an isothermal evolution.

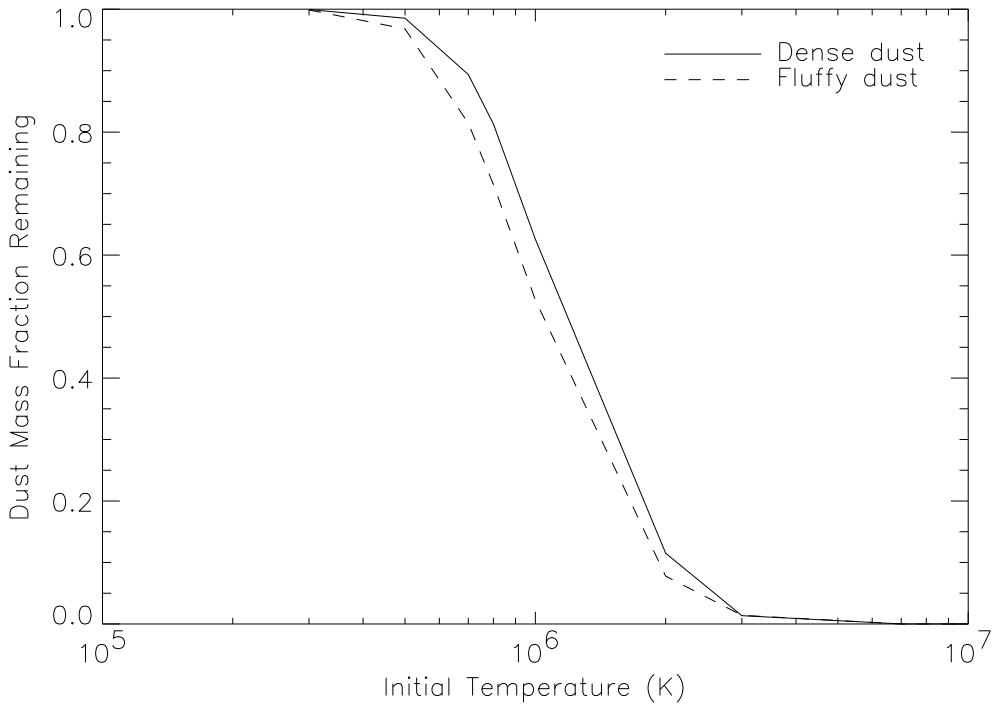

Figure 2.8: Dust mass fraction remaining after cooling to 10^4K as a function of initial temperature.

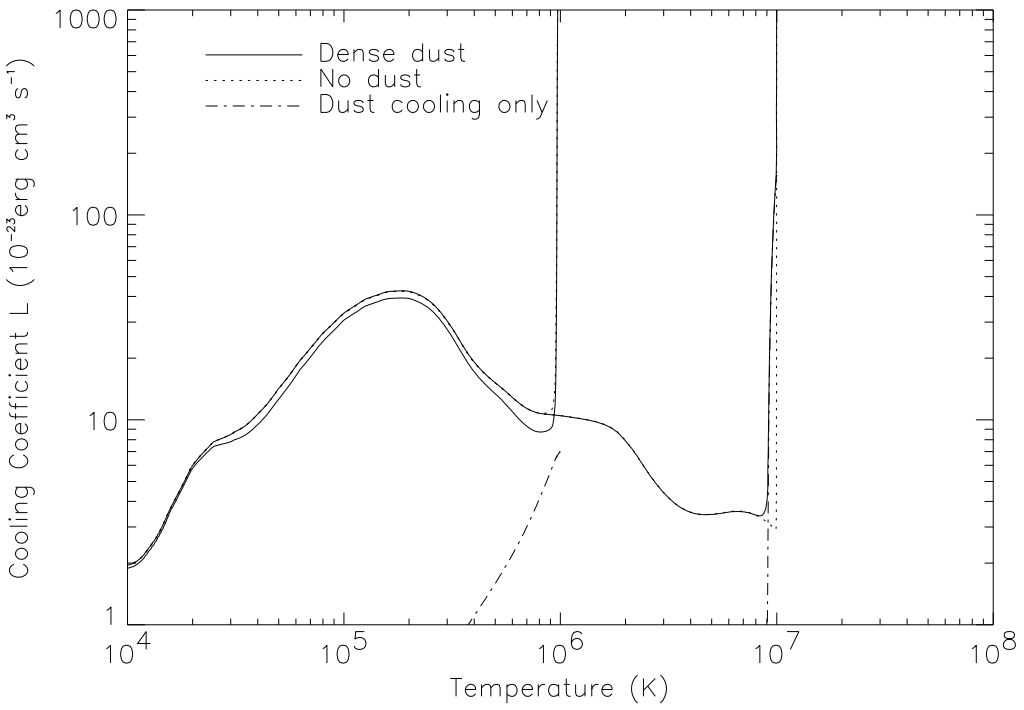

Figure 2.9: Cooling coefficient evolutions for isobaric cooling starting from kinetic temperatures of 10^6K and 10^7K and ionization equilibrium at 2×10^4K. Huge ion flash and dust cooling epoch can easily be distinguished. Dense dust is used.

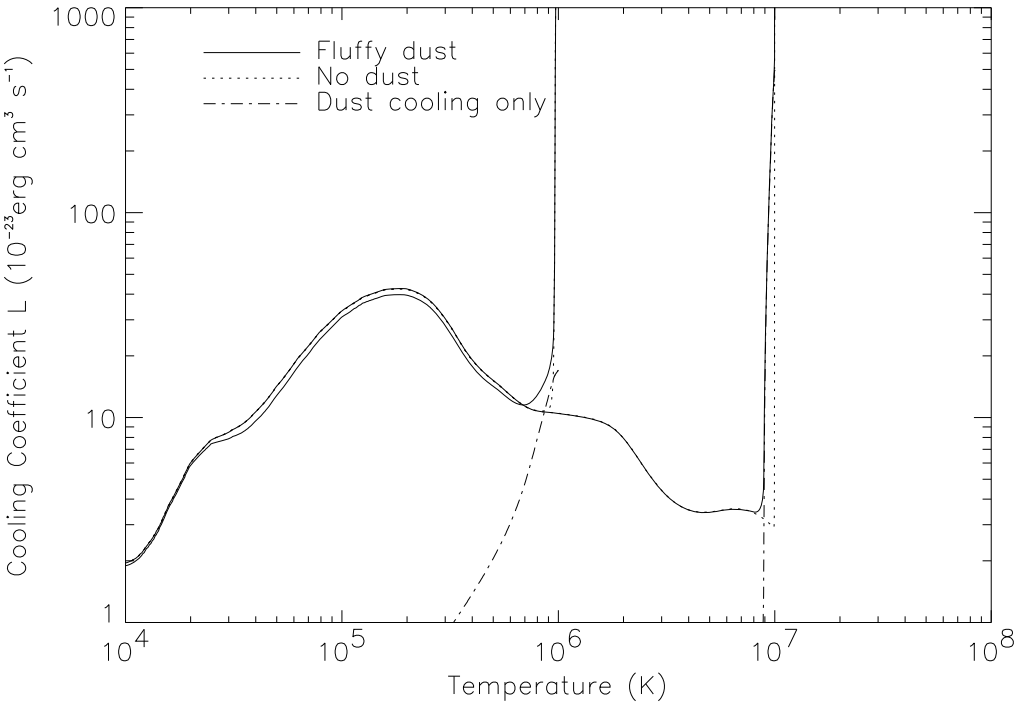

Figure 2.10: Same as Figure 9 but with fluffy dust.

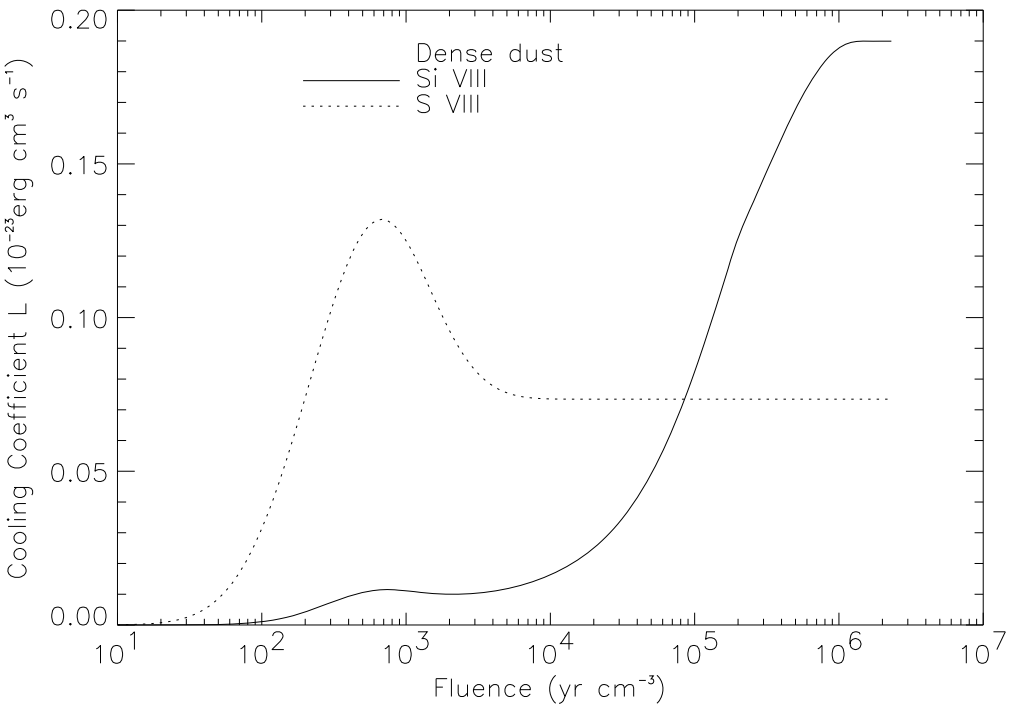

Figure 2.11: Spectral line cooling of Si VIII (λ61Å) and S VIII (λ63.5Å) vs fluence at 10^6K starting from ionization equilibrium at 2×10^4K, with dense dust.

Table 2.1: Depleted Gas and Dust Constituents

	Logarithmic[a]			Parts per million H		
Element	Gas	Silicate	Carbon	Gas	Silicate	Carbon
Carbon	8.40	7.86	7.56	254	72	36
Nitrogen	8.05	—	—	112	0	0
Oxygen	8.83	8.26	—	673	180	0
Neon	8.09	—	—	123	0	0
Magnesium	6.11	7.57	—	1.3	37.1	0
Silicon	6.04	7.54	—	1.1	34.7	0
Sulfur	7.27	—	—	18.5	0	0
Argon	6.56	—	—	3.6	0	0
Calcium	2.60	6.34	—	4×10^{-4}	2.2	0
Iron	5.60	7.50	—	0.4	31.9	0
Nickel	4.00	6.25	—	1×10^{-2}	1.8	0
Aluminum	4.48	6.48	—	3×10^{-3}	3.0	0

[a](where H = 12.00)

Table 2.2: Dust Parameters

Grain Type	A (μm^{p-1} gr/H)	N (gr/H)	M_g (g/H)
Dense Silicates	1.9×10^{-15}	4.8×10^{-12}	1.3×10^{-26}
Fluffy Silicates	3.7×10^{-15}	9.5×10^{-12}	1.3×10^{-26}
Graphite	4.6×10^{-17}	1.0×10^{-11}	7.2×10^{-28}

Table 2.3: Fountain Column Densities (cm^{-2})[b]

Dust	Model	C IV	N V	O VI	Si IV	S IV	S VI
None	Isochoric	9.3(13)	4.6(13)	6.9(14)	5.2(12)	1.2(13)	6.2(12)
None	T_{tr}[4.7]	3.5(13)	2.1(13)	4.3(14)	1.9(12)	4.8(12)	3.3(12)
None	T_{tr}[2.2]	1.9(13)	1.8(13)	4.6(14)	9.3(11)	2.3(12)	3.2(12)
None	Isobaric	1.2(13)	1.7(13)	4.6(14)	3.5(11)	1.4(12)	3.1(12)
Dense	Isochoric	7.5(13)	4.9(13)	6.6(14)	1.7(12)	1.3(13)	6.7(12)
Dense	T_{tr}[4.7]	3.0(13)	2.3(13)	4.3(14)	8.5(11)	5.2(12)	3.7(12)
Dense	T_{tr}[2.2]	1.7(13)	2.0(13)	4.6(14)	4.2(11)	2.5(12)	3.6(12)
Dense	Isobaric	1.1(13)	1.9(13)	4.6(14)	1.7(11)	1.6(12)	3.6(12)
Fluffy	Isochoric	7.5(13)	4.7(13)	6.2(14)	2.1(12)	1.3(13)	6.2(12)
Fluffy	T_{tr}[4.7]	2.9(13)	2.1(13)	3.9(14)	9.6(11)	5.2(12)	3.4(12)
Fluffy	T_{tr}[2.2]	1.6(13)	1.8(13)	4.2(14)	4.8(11)	2.5(12)	3.3(12)
Fluffy	Isobaric	1.0(13)	1.8(13)	4.2(14)	1.9(11)	1.6(12)	3.2(12)

[b]The numbers in ()'s are powers of ten.

References

Anders, E. & Grevesse, N. 1989, Geochimica et Cosmochimica Acta, 53, 197

Arendt, R.G., Dwek, E., & Leisawitz, D. 1992, ApJ, 400, 562

Burke, J. R., & Silk, J. 1974, ApJ, 190, 1

Cui, W. & Cox, D.P. 1992, ApJ, 401, 206

Draine, B. T. & Salpeter, E. E. 1979, ApJ, 231, 438

Dwek, E. 1981, ApJ, 247, 614

Dwek, E. 1987, ApJ, 322, 812

Dwek, E. 1992, private communication

Dwek, E., Petre, R., Szymkowiak, A., & Rice, W. L. 1987, ApJ, 320, L27

Dwek, E., & Smith, R. K. 1995, ApJ, in press

Edgar, R.J., & Chevalier, R.A. 1986, ApJ, 310, L27

Kahn, F.D. 1975, Proc. 15th International Cosmic Ray Conference (Munich), 11, 3566

—— 1976, A&A, 50, 145

Itoh, H. 1989, PASJ, 41, 853

Mathis, J.S. 1992, private communication

Mathis, J.S. 1994, private communication

Mathis, J.S., Cohen, D., Finley, J.P., & Krautter J. 1994, ApJ, submitted

Mathis, J.S., Rumpl, W., & Nordsieck, K.H. 1977, ApJ, 217, 425

Mathis, J.S., & Whiffen, G. 1989, ApJ, 341, 808

McKee, C.F., Hollenbach, D.J., Seab, C.G, & Tielens, A.G.G.M. 1987, ApJ, 318, 674

Ostriker, J. & Silk, J. 1973, ApJ, 184, L113

Raymond, J. C., & Smith, B. W. 1977, ApJS, 35, 419

Raymond, J. C., & Smith, B. W. 1984, private communication

Raymond, J. C., & Smith, B. W. 1993, private communication

Seab, C.G. 1987, in "Interstellar Processes", Hollenbach, D. J. & Thronson, H. A. eds. (Dordrecht:Kluwer) p. 491

Smirnov, V.N., Vaisberg, O.L., & Anisimov, S. 1988, Astr. Ap., 187, 774

Spitzer, L. Jr., & Jenkins, E. B. 1975, ARA&A, 13, 133

Tielens, A.G.G.M., McKee C.F., Seab, C.G., & Hollenbach, D.J. 1994, ApJ, 431, 321

Vancura, O., Raymond, J.C., Dwek, E., Blair, W.P., Long, K.S., & Foster, S. 1994, ApJ, 431, 188

Chapter 3

Modeling the Local Bubble

3.1 Introduction

Observations of the local ISM show the presence of a pervasive hot gas emitting soft X-rays, which must be closer than the nearest $N_H = 10^{19}$ cm^{-2}. (Juda, 1991) From the survey observations (McCammon *et al.* , 1983) we can get the apparent temperature ($\sim 10^6$ K) and emission measure (0.003 cm^{-6} pc) assuming the X-rays are due to an thermal plasma in collisional equilibrium (calculated using the code from Raymond & Smith (1977,1993)). Combining this with the EUV observations that suggest a local cavity of radius 80 pc (Warwick *et al.* , 1993) leads to $\overline{n_e} \sim 0.006$ cm^{-3}. The total energy in the emitting region, given these values, is

$$E_{thermal} = 1.5PV = 1.5\chi nkTV \sim 1.6 \times 10^{50}\text{ergs} \tag{3.1}$$

This amount of energy could come from an OB association, but there are none within 100 pc. The other obvious cause of the hot gas is a supernova explosion, or a series of explosions. If this is so, the relative quiescence of nearby interstellar material suggests that the last supernova was more that 10^6 years ago (Cox & Reynolds, 1987). The single supernova case was considered

by Edgar & Cox (1993) (EC) with partial success. This other possibility, that the Local Bubble is the leftover remnant of a burst of supernovae, will be explored here.

3.2 Methods

A Type II supernova releases 10^{53} ergs of gravitational energy, only $\sim 10^{51}$ ergs of which is converted to the kinetic energy of the explosion. The details of this conversion are quite complex, but are not needed for this problem. As shown below, after 10^4 years only the initial energy input is important. This energy then propagates to the ISM in the form of photons and particles. The density of matter in interstellar space is low enough that the shock is collisionless; the material interacts largely through the magnetic field in the ISM. (Shu, p. 235) Thus, all shocks in the ISM are inherently magnetic, a problem which has complicated and will continue to complicate investigations of supernova remnants.

In order to examine supernova remnant models, therefore, a hydrodynamic shock code is needed. The code must follow the time-dependent heating and cooling of the gas and the possible effects of thermal conduction. EC, using such a code, attempted to model the Local Bubble and found substantial difficulties when using a single supernova explosion into a dust-free ISM. They suggested that multiple supernova explosions, as well as including dust, might be necessary to overcome their problems.

3.2.1 Hydrodynamics

The initial problem in modeling a supernova is following a propagating three-dimensional shock wave. It is necessary, given current computational constraints, to reduce this problem to one dimension by assuming spherical symmetry. The hydrodynamic equations can then be derived by requiring mass conservation, momentum conservation, and energy conservation in an ideal gas (with $\gamma = 5/3$):

$$\frac{d\rho}{dt} = -\nabla \cdot (\rho u) \tag{3.2}$$

$$\rho \frac{du}{dt} = -\nabla (p_{th} + p_{mag}) \tag{3.3}$$

$$\frac{d}{dt}\left(\frac{p_{th}}{\rho^\gamma}\right) = -\frac{(\gamma - 1)}{\rho^\gamma}\epsilon \tag{3.4}$$

where r is the distance from the explosion (centered at $r = 0$), $u = dr/dt$, p_{th} is the thermal pressure in the gas, p_{mag} the magnetic pressure, and ϵ the emissivity of parcel. The magnetic field is assumed to be transverse and "frozen" with the mass, so $p_{mag} = (B_0 n)^2/8\pi$. This approximation was discussed at length in Slavin & Cox (1992).

To solve these equations numerically, a grid of "parcels" is created which covers the spatial range desired. These are then initialized with the desired starting conditions and evolved using first-order approximations to the above equations. The time step is chosen using the Courant condition and the cooling timescale. A Lagrangian formulation, which follows mass parcels, was used. With this method, matter never leaves its initial parcel, which simplifies the calculation of ion states greatly since there is no mixing. The code uses artificial viscous pressure to smear the shock front, based on the method of Richtmyer & Morton (1967).

The biggest complication in solving these equations is the calculation of ϵ, the emissivity of a parcel. In the most general form,

$$\epsilon = n_e n_H (L_{gas} + L_{dust}) + \nabla \cdot F_c \tag{3.5}$$

where n_e and n_H are the electron and hydrogen densities, L_{gas} and L_{dust} the gas and dust cooling coefficients, and $\nabla \cdot F_c$ the divergence of the thermal conduction flux. In the hot region of the supernova remnant, the gas cools by radiation associated with collisional excitation and recombination of the ions. L_{gas} is calculated by a table-driven version (Edgar, 1993) of the Raymond & Smith (1977, 1993) code. The Edgar code calculates the cooling of the gas and follows the ionic abundances, but to save time does not calculate the spectrum emitted. The dust cooling, L_{dust}, is calculated by the method and program described in Chapter 2. As the dust sputters, it is returned to the gas phase as neutral atoms which are subsequently evolved by the gas cooling code. The emission from gas and dust leaves the system; thermal conduction, however, only transfers energy between parcels. This can have a very significant effect on the resulting structure.

3.2.2 Thermal Conduction

Classical thermal conduction in a fully-ionized plasma has been described by Spitzer (1956) to follow the form

$$F_{cla} = -\kappa(T)\frac{dT}{dr} \tag{3.6}$$

with $\kappa(T) = \beta T^{5/2}\cos^2\theta$. θ is the angle between the magnetic field and radial direction, and β is approximately constant (6×10^{-7}erg cm^{-1}s^{-1}K$^{-3.5}$), for

temperatures above 10^5K. The $\cos^2\theta$ term here (and the $\cos\theta$ term in saturated conduction below) attempts to model the reduced thermal conduction due to the magnetic field (see Slavin, 1989). The energy transfer due to thermal conduction is just the divergence of this flux, $\nabla \cdot F_{cla}$. However, the flux is limited by saturation. Thermal conduction cannot transport energy faster than the energy in the conducting particles times their mean speed: $E_{thermal} \cdot \overline{v}_{rms}$. The saturation limit is further reduced by the requirement of charge neutrality. The code follows Cowie & McKee (1977) for the flux in the saturated case:

$$F_{sat} = -\Big(sign\Big(\frac{\partial T}{\partial r}\Big)\Big)\, 5\cos\theta\, \phi_s \cos\theta\, \rho\, c^3 \tag{3.7}$$

where c is the isothermal sound speed and ϕ_s is a "saturation parameter," taken to be 0.3. Assuming cosmic abundances of hydrogen and helium, fully-ionized, equation 3.7 is equivalent to

$$F_{sat} = -\Big(sign\Big(\frac{\partial T}{\partial r}\Big)\Big)\, 4.5\cos\theta\, n\Big(\frac{k_B T}{m}\Big)^{1/2} k_B T \tag{3.8}$$

The classical and saturated fluxes should be combined in a smooth way. The final form used in the hydrocode follows Cowie (1977):

$$F_{total} = \frac{1}{\frac{1}{F_{cla}} + \frac{1}{F_{sat}}} \tag{3.9}$$

3.2.3 Tests

The hydrocode was tested against a number of analytic and numerical standards. The dynamical evolution was tested in two different ways. In one dimension, the code correctly solved the Riemann shock tube problem. In three dimensions, the code reproduced the Sedov (1959) solution to a spherically symmetric point-explosion. In order to test the cooling functions, the X-ray

emission from collisional excitations of the gas in equilibrium was checked by matching the emission generated by the equilibrium Raymond & Smith model in XSPEC (Arnaud, 1995).

To test the code's overall performance, sample runs were compared to results from the hydrocode written by Miller (1994), which uses a similar technique but was written independently. An example described by EC was also run and both the hydrodynamics and the predicted emission matched their results.

3.3 Supernova Explosions

A supernova explosion is a fantastically complicated process with timescales ranging from microseconds to millions of years. At early times, the stellar conditions dominate, but the late-term evolution of the supernova remnant depends largely on the characteristics of the interstellar medium around the star. After 10^4 years, many of the details of the stellar explosion combine into a few parameters important to the long term SNR evolution: the initial energy ($\sim 10^{51}$ ergs) and, to a lesser extent, the mass of the ejecta ($\sim$ few $M_\odot$).

3.3.1 Initial Conditions

Two types of initial conditions are considered in this modeling effort: a hot start, where the ejected mass in a specified volume is given the thermal energy of the supernova; and a cold start, where the mass and initial volume is given and a velocity gradient assumed such that the total kinetic energy of the volume is equal to the supernova energy.

Table 3.1: Initial Ejecta Parameters

		Input		Resulting Peak	
Case	Mass ($M_\odot$)	Radius (pc)	Type	Position (pc)	n (cm^{-3})
1	1.0	1.0	Kinetic	8.53	17.1
2	1.0	1.0	Thermal	8.37	17.0
3	1.0	3.0	Kinetic	8.77	17.0
4	1.0	3.0	Thermal	8.49	17.1
5	3.0	1.0	Kinetic	8.55	17.1
6	3.0	1.0	Thermal	8.35	17.1
7	3.0	3.0	Kinetic	8.87	17.0
8	3.0	3.0	Thermal	8.50	16.9

In a hot start, the pressure inside the "ejecta" is much greater than the surroundings, and the ejecta rapidly expands. In the cold start, the ejecta expands rapidly, forming a reverse shock that propagates through and heats the ejecta. The resultant remnants become similar rapidly. Eight different initial conditions, with the peak density and shock position at 10,000 years, are given in Table 3.1 and the results for 4 extreme cases are shown in Figure 3.1. The variation between these models at 10,000 years is only 6% in the shock position and 1% in peak density, and becomes smaller as time progresses.

3.3.2 Multiple Explosions

Multiple supernova explosions in a one-dimensional Lagrangian hydrocode create two issues that must be considered: code geometry and ejecta mass. First, all explosions must begin at the center of the previous explosion. The new shock wave will travel rapidly through the low-density interior of the remnant until it reaches the previous shock or wall, where it merges. An off-center

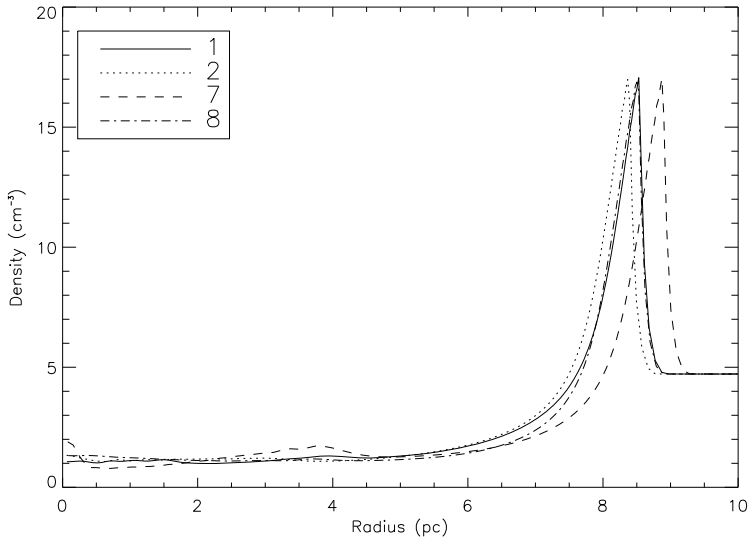

Figure 3.1: Density vs radius at 10,000 years with many differing initial conditions

second supernova shock in a three-dimensional code should hit one one side of the remnant first and slow down allowing the remaining shock to pass quickly through the rest of the remnant. A measure of the actual effect of non-centered supernovae would be useful.

The other issue is that the ejected mass of a second supernova cannot be easily added to the hydrocode after the first explosion. The Lagrangian formulation follows the mass in each parcel, and so assumes the mass in each cell to be constant. Adding mass post-initialization requires either mixing mass between cells or arbitrarily moving it to create space. Another possibility would be to add the energy of the supernova to some central zones in the remnant in the form of kinetic or thermal energy. In this case, since the density in the center of the remnant will in general be very low, either the ejecta mass of the supernova will be small or the initial radius will be very

large. Figure 3.1 shows that small variations in initial conditions do not matter significantly, but not for an ejecta mass of only .01 $M_{\odot}$ or initial radius of 20 pc.

A solution to this issue is to "pre-load" the initial cells with as many supernovae as needed. For example, three supernovae can be placed in the hydrocode with any desired mass and radius before calculations are begun. Supernova #1 exists between 0 and r_0, #2 between r_0 and r_1, and #3 between r_1 and r_2. The interior boundary is set to r_1 and the first supernova (#3) explodes outwards (with a hard core of radius r_1 at the center). Whenever desired, the interior boundary is moved inward to r_0, and the second supernova is released. Finally, setting the boundary to 0 allows the third supernova to escape. This method allows for any reasonable number of supernovae to be generated, as long as the initial outer radius r_i is much smaller than the radii of interest. A test showed almost identical results between a run with initial boundary at 0 pc and one starting at 1 pc.

3.3.3 Sample Bubble Evolution

Several sample models, with a range of initial parameters, were run to explore the parameter space available (see Table 3.2). The results were surprisingly uniform, varying only slightly with relatively large changes in the initial conditions. Two cases from Table 3.2, A and F, will be discussed in depth.

Two Explosions

Model A has initial conditions of a temperature of 2.2×10^4K, a density of 0.2 nuclei/cm^{-3}, and a magnetic field of 5 μG. Two supernovae, each with energy

Table 3.2: Model Parameters

Model	Description
A	Standard 2 SN explosion
B	A, except $\beta = \beta_0/3$
C	A, except $E_0 = 10^{51}$ ergs
D	A, with dust included
E	A, with a third SN at 3 Myr
F	E, except $\beta = \beta_0/3$
G	E, except $\beta = \beta_0/30$
H	E, with dust included

0.5×10^{51} ergs and spaced 10^6 years apart, are then exploded into this ISM. The first explosion forms a bubble with a 60 pc radius and central temperature of 5.5×10^5 K in 1 Myr. The bubble is then reheated, temporarily, by the second explosion. After 2 Myr, it has expanded to its maximum radius of 84 pc and cooled to 7.3×10^5 K. At this point, the interior pressure (p/k) is approximately 7000 $cm^{-3}K$, and the gas inside the bubble has velocities less than 5 km/s.

The bubble then begins a slow collapse. The temperature profile contracts in a nearly self-similar manner, retaining the shape shown in Figure 3.2. The bubble radius initially contracts at rate of 5 km/s, slowly increasing to $\sim$ 12 km/s although the central temperature remains constant, as shown in Figure 3.3. The total mass of hot ($\geq 10^5$ K) gas does decrease, nearly linearly, dropping from 500 $M_\odot$ to zero. The interior pressure remains constant at 7000 $cm^{-3}K$ until 6 Myr, when it begins to rise linearly at a rate of 10,000 $cm^{-3}K$ per Myr.

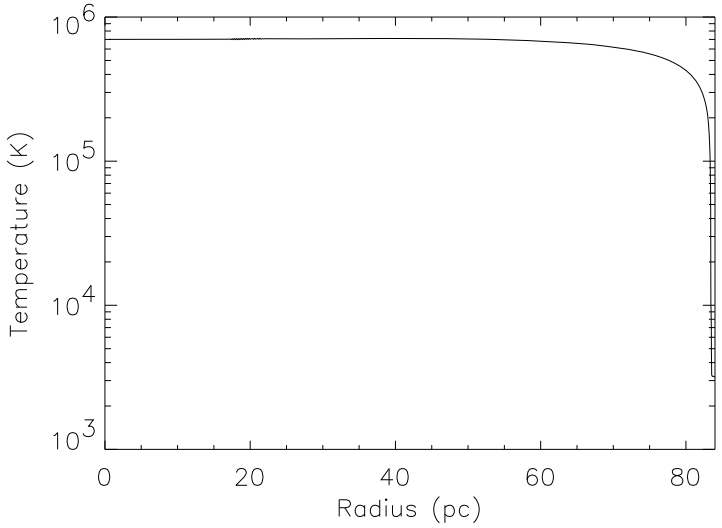

Figure 3.2: Bubble Temperature vs Radius at 3 Myr in Model A

Three Explosions

Model F is similar to the above, with two important differences. The first is the third explosion, 2 Myr after the second one, and the second is that the thermal conduction strength is reduced by one-third. The spacing was chosen to catch the bubble after it had reached peak size and just begun to contract, so that the effect of the third explosion on the maximum bubble radius could be clearly seen. The efficiency of thermal conduction was reduced to explore how such variations (which might be expected due to magnetic fields restricting the motion of the energy-conducting particles) effect the results.

The results are somewhat similar to the two explosion case. At 3 Myr, the bubble has about the same radius as the two explosion model, although the pressure in the bubble is higher, 11,500 $cm^{-3}K$. After the third explosion the bubble expands, reaching a maximum size of 96 pc at 4.5 Myr. The bubble

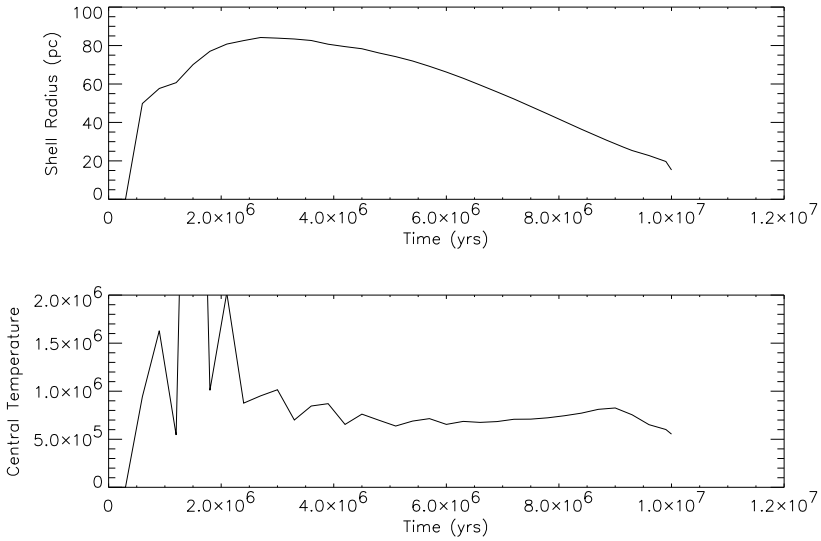

Figure 3.3: Bubble Radius and Temperature vs Age

radius then contracts linearly at 6 km/s. The central pressure follows the pattern as the two explosion case, remaining nearly constant for a long period and then rising linearly. However, the constant pressure remains at 11,500 $cm^{-3}K$, much higher than in model A and when it begins to rise linearly (at 7 Myr) the rate is much slower, only 1300 $cm^{-3}K$ per Myr. The central temperature, while constant like the two explosion case, is 1.2×10^6 K, also much higher than before. The increase in pressure and temperature is largely due to the decrease in the thermal conductivity; an identical run (model E) with normal conductivity had a constant pressure of 8200 $cm^{-3}K$ and a central temperature of 8.4×10^5 K. Despite the change in pressure and central temperature, the temperature profile retained the same self-similar shape as the two explosion case throughout (see Figure 3.2).

It is also possible to calculate some observable characteristics from these models, such as X-ray band count rates. Figure 3.4 shows the B and C band

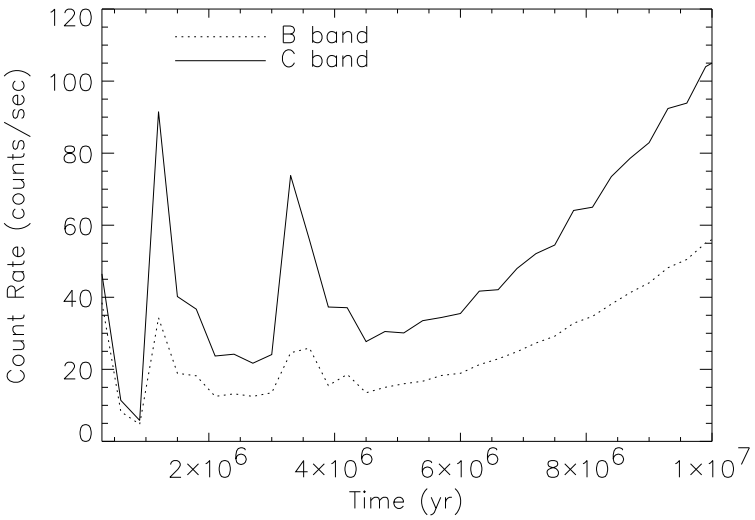

Figure 3.4: B, C Band Count Rate vs Time in Model F

count rates for model F; the sharp peaks are the result of the second and third explosions. Note that the C band rate is everywhere too dim, never even reaching the rate of 125 counts/sec in the plane. The C/B is also too low, remaining slightly below 2 once past the third explosion. This is, however, better than the result in Model A, where the C/B ratio never exceeds 1.5 past the second explosion.

Explosion Characteristics

While various parameters differ, the overall shape and evolution of the bubble is the same for each model. Each explosion increased the size of the bubble; after the last explosion, the bubble radius contracts at a constant rate. The temperature profile $T(r)$ is self-similar for all models A-H, depending only upon the value of the central temperature (T_c) and the bubble radius (R_s). The values of these parameters also show remarkable regularity. In all the

Table 3.3: Explosion Evolution Characteristics

Model	$T_c(10^6)$K	R_{max} (pc)	dR/dt (km/s)	$\overline{p_{int}/k}$ (cm^{-3}K)
A	0.7	83	-10	7.0×10^3
B	1.1	86	- 8	8.0×10^3
C	0.8	105	-12	6.4×10^3
D	0.7	82	-11	8.0×10^3
E	0.7	94	-10	8.6×10^3
F	1.1	96	- 6	1.1×10^4
G	2.3	106	- 5	1.1×10^4
H	0.7	95	-10	9.2×10^3

models with normal thermal conduction, the collapse rate is about 11 km/s, and the central temperature is constant at $\sim 7.5{\times}10^5$ K during bubble collapse. The exceptions here are the models where the thermal conduction constant β is reduced.

These results do differ from single explosion models, mostly in bubble size and collapse rate. A single explosion model identical to model A except with a single explosion with 10^{51} ergs of energy reached a maximum size of only 66 pc, which corresponds to only half the hot volume obtained by model A. In order to reach ~ 100 pc, the EC model required a much greater 5×10^{51} ergs, although admittedly this model also had a substantially increased external pressure. Interestingly, both of these single explosion models collapsed at ~ 20 km/s, much faster than any of the multiple explosion models.

It is possible to draw a number of preliminary conclusions from these results:

- The central temperature of a hot bubble remains constant during bubble collapse.

- The central temperature is independent of explosion energy or number,

but does depend on the thermal conduction and possibly external pressure.

- The internal pressure increases with the number of explosions and possibly with reduced thermal conduction.
- All these models are too dim and too soft in the relevant X-ray bands.

3.4 Analytic results

The specific goal of this project is to model the observed SXRB with the emission from a supernova-created hot gas remnant. With the vast range of parameters (initial density, pressure, thermal conduction suppression, and supernova energy, multiplicity and spacing among others) available, a blind search for a model which describes the SXRB is impractical. The initial trial runs, as shown above, show substantial regularity. In general, these results were too cool and too diffuse; Snowden *et al.* (1990) showed that temperatures closer to 10^6 K are required. The X-ray emission is determined by three parameters, if dust is ignored (as it will be in this section): the electron temperature and density, and the densities of the various ion states. The ion state density is a very complex time-dependent function; the other two parameters, however, appear to be relatively simple.

3.4.1 Differential Emission Measure (DEM)

The edge structure seen in Figure 3.2 recurs in all the model runs. The temperature drops rapidly from above 10^5K to about 10^4K. This is clearly due

to the large increase in the cooling function around 10^5K (see Figure 2.2), partially modified by the rate thermal conduction can transport energy to the edge. It is possible to derive a simple analytic form for this, called here the Differential Emission Measure and defined as $n_e^2 dr/dT$, by balancing thermal conduction and cooling at the edge of the remnant.

To derive the DEM, assume the remnant is large (to minimize dimensional effects), dust-free, isobaric and in steady state. Assume as well that the dominant energy transport mechanisms are thermal conduction and radiation, *i.e.* the convective flux is small.

Basic Equations

In steady state, the energy flux from thermal conduction arriving at a given point is exactly balanced by the radiation emitted at that point:

$$-\nabla \cdot F_{tc} = n_e n_H L(T) \tag{3.10}$$

where $L(T)$ is the gas cooling coefficient, given here by the approximate formula due to Kahn (1975, 1976): $L(T) = \alpha T^{-1/2}$, where $\alpha = 1.3 \times 10^{-19}$ erg cm^3 s^{-1} K$^{1/2}$. F_{tc} is the thermal conduction flux, given in equation 3.9. It is possible to simplify 3.6–3.8 and thus 3.9 further, since the angle θ between the radial coordinate and the magnetic field at the dense edge of the remnant will be nearly $\pi/4$, *i.e.*, the magnetic field will be nearly perpendicular to the direction of supernova explosion. In this case, $\cos\theta \propto 1/n \propto T$, and so equations 3.6 and 3.8 become:

$$F_{cla} \approx -\frac{2}{7}\beta\Big(\frac{T}{T_0}\Big)^2 \frac{\partial}{\partial r}\Big(T^{7/2}\Big) \tag{3.11}$$

$$F_{sat} \approx -4.5p\Big(\frac{T}{T_0}\Big)\Big(\frac{k_B T}{m}\Big)^{1/2} \tag{3.12}$$

for some characteristic temperature $T_0 \gg T$. Dealing with each case individually is easier than using the combined form of 3.9, as shown below.

Classical Thermal Conduction

Define E(T) to be the pressure-normalized DEM:

$$E(T) \equiv -\frac{n_e^2}{(n_e T)}\frac{dr}{dT} \tag{3.13}$$

In the one-dimensional case, then,

$$F_{cla} = -\kappa(T)\frac{dT}{dr} = \frac{\kappa(T)n_e^2}{(n_e T)E(T)} = \frac{\kappa(T)(n_e T)}{T^2 E(T)} \tag{3.14}$$

Substituting this form into 3.10 leads to

$$n_e n_H L(T) = -\frac{dT}{dr}\frac{d}{dT}\Big\{\frac{\kappa(T)(n_e T)}{T^2 E(T)}\Big\} \tag{3.15}$$

and with some algebraic manipulation gives

$$\frac{\kappa(T)L(T)}{T^2}\Big(\frac{n_H}{n_e}\Big) = \frac{d}{dT}\Big\{\frac{1}{2}\Big(\frac{\kappa(T)}{T^2 E(T)}\Big)^2\Big\} \tag{3.16}$$

The final form is then

$$E(T) = \frac{\kappa(T)/T^2}{\sqrt{2\frac{n_H}{n_e}\int_0^T \frac{\kappa(T)L(T)}{T^2}}} \tag{3.17}$$

This form has the advantage that it can be easily evaluated for many different choices of $L(T)$ and $\kappa(T)$. In the pure classical form, with Kahn cooling, $\cos\theta \equiv 1$, and assuming $n_H = n_e$, $E(T) = \sqrt{\beta/(2\alpha)}$. If $\cos\theta$ is small, *i.e.* $T \ll T_0$, $E(T) = \sqrt{3\beta/(2\alpha)}(T_0/T)$. $E(T)$ can be solved in the general case for arbitrary $\cos\theta$ as well.

In the simplest case, the DEM is a constant, independent of T except for how far it extend in T, and is proportional to the pressure. This suggests that

the value of the central temperature and the magnitude of the interior pressure are likely to be the dominant parameters controlling the surface brightness of the x-ray emission.

Saturated

The above solution assumes that the dominant flux at the edge of the remnant is due to classical thermal conduction. It is easy to show that this is true, by calculating the ratio of the saturated flux to the classical flux.

$$\frac{F_{sat}}{F_{cla}} = \frac{4.5p(\frac{T}{T_0})\sqrt{\frac{kT}{m}}}{\beta(\frac{T}{T_0})^2 T^{5/2}\frac{\partial r}{\partial T}} \tag{3.18}$$

$$= \frac{4.5\chi k\sqrt{k/m}}{\beta(nT)}(\frac{T_0}{T})n_e^2\frac{\partial r}{\partial T} \tag{3.19}$$

Substituting the appropriate DEM, $\sqrt{3\beta/2\alpha}(T_0/T)$ into the above shows that $F_{sat}/F_{cla} \gg 1$ when $T \ll T_0$. So the saturation limit is everywhere substantially larger than the classical thermal conduction.

Comparing with Model Calculations

The true test is to see if the analytic DEM correctly predicts the value of $n_e^2\,\partial r/\partial T$ that the hydrocode calculates. The derivation of the DEM assumes the hot bubble is large, isobaric, and stable. In many multiple explosion models there is a long period where these conditions are roughly met, and in these regions, the DEM prediction is usually within 50% of the measured value at the edge. A typical result (from Model E at 5.7 Myr) using unsupressed thermal conduction is shown in Figure 3.5, plotted against temperature. This expands the edge structure, and compresses the hot interior which has a nearly flat

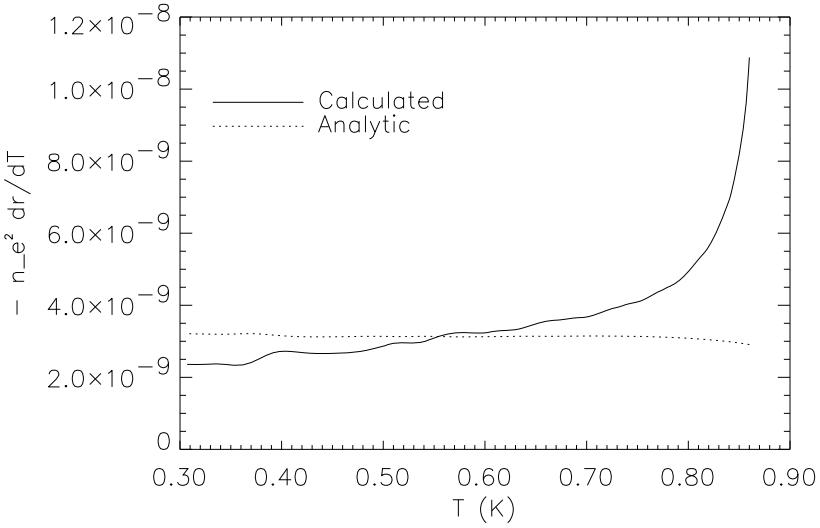

Figure 3.5: Analytic DEM compared to calculated value. Plotted against temperature to expand edge structure

temperature of $\sim 8.5 \times 10^5$ K. Ignoring the divergence at high temperatures (which are far from the edge), there is good correspondence between the two values. Comparisons for models with suppressed thermal conduction and models with different values for α also agreed with the analytical prediction at the same level as shown in Figure 3.5.

3.4.2 Thermal Conduction Driven (TCD) Bubble Models

While the DEM is very successful for estimating the shape of the edge of the bubble, it is not very useful for the interior of the bubble. Energy transfer in the center must be mostly influenced by thermal conduction, since cooling is strongly suppressed by its n^2 dependence, whereas the thermal conduction has a $T^{2.5}$ dependence (see equation 3.6) and so should dominate the internal

energy flow. Finally, this attempt is motivated by the simplicity and regularity of the temperature curves in Figure 3.2, which suggests the bubble interior is relatively unchanged by parameter variations.

Derivation

Substantial assumptions are necessary to begin. The bubble must be stable (*i.e.* constant radius), isobaric, and all energy flux out of the bubble is due to classical thermal conduction. Since energy will flow out of the bubble, the internal pressure will drop unless replenished. However, there is an energy source, supernovae, which are assumed to explode with a regular period τ_{sn} and spread their energy equally throughout the bubble. Cooling is ignored inside the bubble.

With these assumptions, energy balance requires that

$$\frac{d}{dt}\Big(\frac{3}{2}pV\Big) = 4\pi r^2 F_{cla} \tag{3.20}$$

The time dependence must be eliminated from the derivative in equation 3.20. Although $dV/dt \equiv 0$ by prior assumption, the simplest course for dp/dt is to assume that for some τ,

$$\frac{d}{dt}\Big(\frac{3}{2}pV\Big) = \frac{3}{2}V\frac{dp}{dt} \sim \frac{3}{2}V\frac{p}{\tau} \tag{3.21}$$

Combining equations 3.20 and 3.21, with some manipulation, gives the result

$$\int_0^r -\frac{p}{\tau}\, r\, dr = \int_{T_c}^{T} 2\beta\, T^{2.5}\, dT \tag{3.22}$$

which then gives the final solution, for some central temperature T_c and some bubble radius R_s,

$$T(r) = T_c(1 - (r/R_s)^2)^{2/7} \tag{3.23}$$

The central temperature T_c and bubble radius R_s should be calculable from the input energy E_{sn}/τ_{sn} and the external pressure p. To find these relationships, three equations will be necessary. The first comes from the assumption of a steady-state bubble, balancing the energy input and output rates:

$$E_{sn}/\tau_{sn} = 1.5\, p\, V/\tau \tag{3.24}$$

The second relationship between these variables comes from integrating equation 3.22 over the entire bubble:

$$R_s = \sqrt{\frac{8\,\beta\,\tau}{7\,p}}\, T_c^{7/4} \tag{3.25}$$

The last relationship can be found by requiring that the total energy loss in the bubble be due to cooling alone, since thermal conduction can only move energy. Using the differential emission measure to simplify the equations:

$$-\frac{d}{dt}(\frac{3}{2}\,p\,V) = 4\,\pi\,R_s^2 \int_0^{T_c} n_e^2 \frac{dr}{dT} L(T) dT \tag{3.26}$$

$$= 4\,\pi\,R_s^2 \int_0^{T_c} \sqrt{\frac{\beta}{2\alpha}}(n\,T)\frac{\alpha}{\sqrt{T}} dT \tag{3.27}$$

Which can be integrated to yield the final relation

$$\tau = \frac{k\,R_s}{\sqrt{2\,\alpha\,\beta\,T_c}} \tag{3.28}$$

These three equations, 3.24, 3.25, and 3.28 can now be manipulated to yield the central temperature and radius of the steady-state bubble:

$$T_c = \Big[\frac{49}{128\pi\,\beta}\sqrt{\frac{2\alpha}{\beta}}\frac{E_0}{\tau_{sn}}\frac{p}{k}\Big]^{2/13} \tag{3.29}$$

$$= 1.78 \times 10^6 \mathrm{K}\,\Big[\frac{E_{51}}{\tau_{sn\,6}}(\frac{p}{k})_4\Big]^{2/13} \tag{3.30}$$

$$R_s = \left(\frac{8}{7}\right)^{1/13}\left(\frac{\beta}{2\alpha}\right)^{7/26}(2\,\pi\,\beta)^{-6/13}(\frac{p}{k})^{-7/13}(\frac{E_0}{\tau_{sn}})^{-7/13} \quad (3.31)$$

$$= 317\text{pc}\left(\frac{E_{51}}{\tau_{sn\,6}}\right)^{6/13}\left(\frac{p}{k}\right)_4^{-7/13} \quad (3.32)$$

Comparing with Model Calculation

Only energy considerations are used to derive the TCD bubble model; all hydrodynamic effects are ignored. As a result, the model should only be compared to the late-term evolution of hot bubbles, at least 1 Myr after the last explosion.

The obvious way of testing the TCD model is to examine a series of equally spaced equal-size explosions, and ask if the results fit the model. Since this is a slow process, only one such run could be done, with equilibrium cooling only. The run had seven explosions, with $E_0 = 0.5 \times 10^{51}$ ergs spaced every 0.5 Myr in a uniform ISM with pressure 2.1×10^4 cm^{-3}K. The results were positive but not confirming. The central temperature, expected to be $\sim 2 \times 10^6$K, varied about this value, never quite settling down. The bubble radius was also too small, reaching a maximum size of 138 pc soon after the seventh explosion, much less than the 212 pc predicted.

The local bubble need not be the product of equally spaced explosions, however. The energy input from supernova explosions in the model serves to keep the bubbles "inflated." A partially inflated bubble is much more likely in reality, the result of a supernova explosion coincidentally occurring inside an old SNR. In this case, the shell radius will certainly be less than predicted, and it is not clear what energy luminosity to use to calculate T_c. However, the temperature distribution itself depends on the balance of cooling and thermal

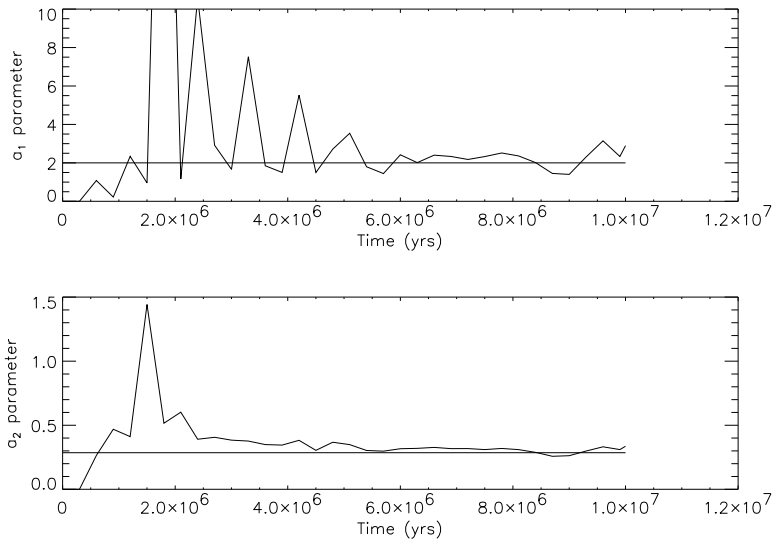

Figure 3.6: Comparing the TCD model with calculations

conduction, scaling linearly with T_c and R_s. Additionally, the temperature distribution was observed to follow a self-similar solution in trial runs. The function

$$T(r) = T_c(1 - (r/R_s)^{a_1})^{a_2} \tag{3.33}$$

was used to fit the temperature in the sample runs, with the central temperature and shell radius taken from the data. The parameters a_1 and a_2 were allowed to float freely in order to get the best fit to each temperature curve. The fits are in general excellent, consistently within 10% of the observed value at all points, and usually within 5%. The values of the fit parameters a_1 and a_2 for the sample run are shown in Figure 3.6. This result is characteristic of all the models examined; the parameters initially oscillate and then tend towards the predicted values of 2 and 2/7, respectively

Even with $T(r)$ known, however, the bubble radius and central temperature must be set. As Table 3.3 showed, the bubble radius is easily attainable with reasonable parameters. The central temperature of the bubble, however, tended to be too cool. T_c is not strongly affected by dust or the supernova energy; only changing the external pressure or the value of the thermal conduction constant β had an effect. The TCD model predicts this effect; it is easy to see from the derivation that

$$T_c = T_{c0}\Big(\frac{\beta}{\beta_0}\Big)^{-3/13} \tag{3.34}$$

To test this, a series of single supernova explosions with varying β was calculated. The resulting values of T_c, shown in Figure 3.7, is fit very well with a power of -0.271, or -3.5/13. Interestingly, since the classical thermal conduction flux is $\propto T^{7/2}$, this result implies that the thermal conduction flux is actually *independent* of β, despite the appearance of equation 3.6. Although there is no physical reason β should be reduced in the ISM, this result shows the importance of thermal conduction in determining T_c. However, there was no corresponding change in the bubble pressure in these runs, which is also apparent from Table 3.3.

3.4.3 Using the Analytic Results

The DEM and the extension of it to the TCD model predict temperature distributions well, and so should be usable for predicting the emission from a hot bubble. Since the objective is to find a model that will have the observed size and X-ray emission of the Local Bubble, it is now imperative to examine the characteristics of the emission using the temperature curve from the TCD

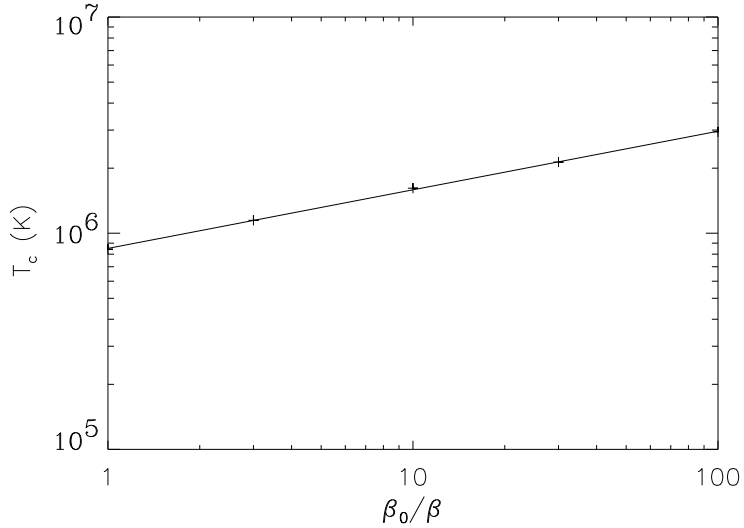

Figure 3.7: Central bubble temperature vs β

model. In equilibrium, it is possible to define functions $B_{em}(T)$ and $C_{em}(T)$, the B and C band counts per second per emission measure. Assuming the bubble is isobaric with pressure p, and the temperature distribution is of the form $T(r) = T_c(1-(r/R_s)^2)^{2/7}$, the total B band count rate from a hot bubble is:

$$B(T_c, R_s, p) = R_s(p/\chi k)^2 \int_0^1 \frac{B_{em}(T(r))}{T(r)^2} dr \tag{3.35}$$

and a similar equation can be written for the C band counts.

Using equation 3.35, it is possible to find the emission, in equilibrium, from a bubble of any size, pressure, and central temperature. Figure 3.8 shows the B and C equilibrium emission as a function of central temperature for a bubble of radius 100 pc and pressure 10^4 cm^{-3}K. Figure 3.9 plots the C/B ratio versus central temperature; this graph is independent of bubble radius and pressure, and so unambiguously determines the central temperature necessary for a given

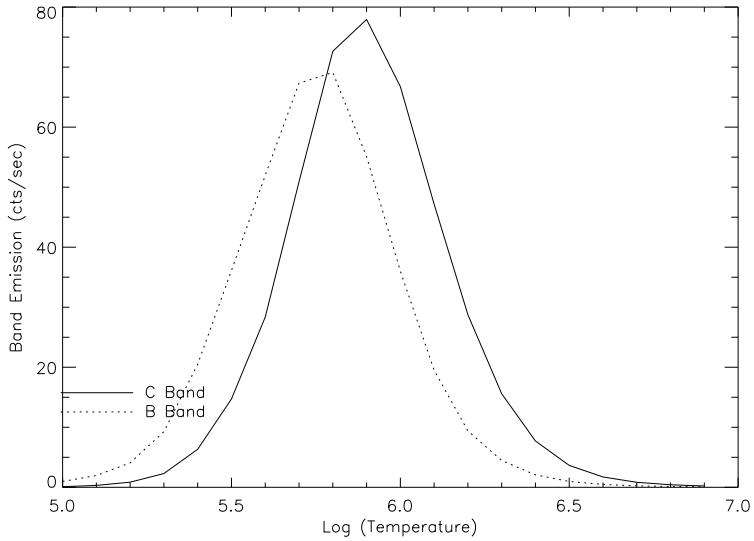

Figure 3.8: B and C Band Emission versus Central Temperature

C/B ratio. The observed value is C/B ~ 2.5, which implies $T_c \approx 1.3 \times 10^6$K. The values of a_1 and a_2 do vary in the fits to the data, however, so it is important to understand the stability of this result to variations in the form of $T(r)$. To explore this possibility a similar analysis was done over the entire range of values found for these parameters, and the result was that the value of T_c necessary for a C/B ratio of 2.5 varied between 1–2$\times 10^6$K. This was deemed to be acceptably stable, so the analytic predictions ($a_1 = 2, a_2 = 2/7$) for the parameters are used exclusively in the following. With the central temperature set by the C/B ratio, and the radius set by EUV measurements to be 70–100 pc, it is possible to uniquely determine the bubble pressure necessary to get the emission. For a C band rate of 125 counts/sec, $\overline{p} = 16,500 - 19,700$ cm^{-3}K.

However, the only direct way to increase the pressure inside the bubble is to have a higher exterior pressure. Increasing the number of explosions does seem to increase the interior pressure, but in general the exterior pressure is

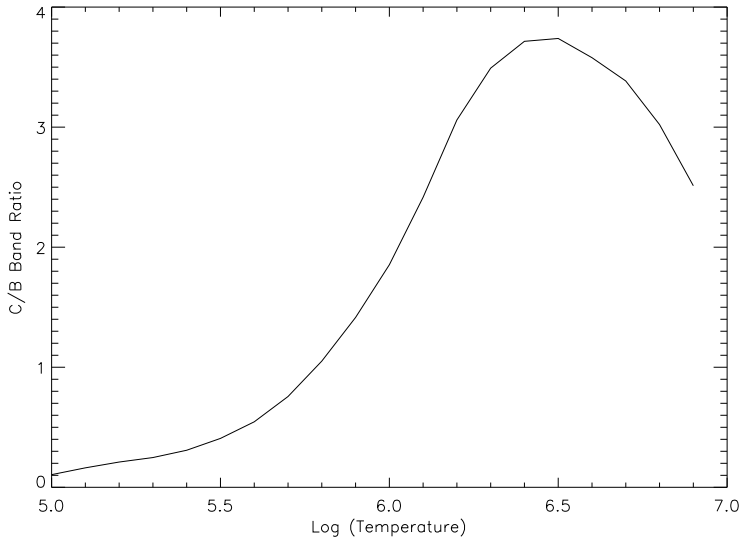

Figure 3.9: C/B band ratio versus central temperature

greater than the interior. This must occur in order to start the collapse of the bubble. We are therefore back in the bind first found by EC: in order to create sufficient emission, the pressure in the ISM may need to be very high, possibly unrealistically so.

This prediction is only useful, however, if the actual non-equilibrium rates are close to the equilibrium rates during the slow bubble collapse time. Figure 3.10 shows the equilibrium B and C band emission, calculated from the density and temperature curves in model F, along with the calculated B and C rates using the Raymond & Smith (1993) code. The non-equilibrium tends to be below the equilibrium, but does track it, getting closer to the equilibrium emission at later times as would be expected. This result holds true for all the models, so it is reasonable to use the equilibrium rates if it is remembered that they will tend to modestly overstate the calculated emission. This, in turn, worsens the pressure problem since it implies an even higher pressure will be

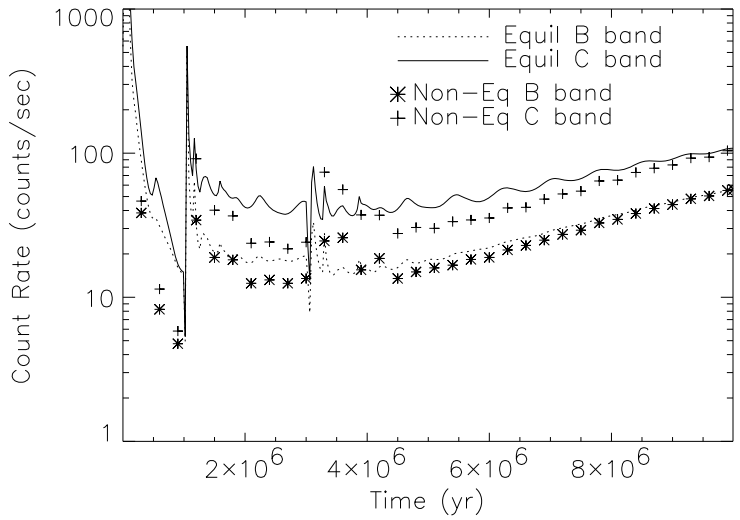

Figure 3.10: Comparison of equilibrium and non-equilibrium B and C band emission for Model F.

needed to get the desired emission.

Another result to be considered is the implications of equation 3.35 for the emissivity. This type of model may be consistent with the displacement scenario, since it implies the x-ray count rates are proportional to bubble radius. Figure 3.11 shows the running integral of the equilibrium B and C band surface brightnesses versus radius, for a bubble with a total radius of 100 pc and with the standard $T(r)$ curve, pressure $= 10^4$ cm^{-3}K, and $T_c = 1.3\times10^6$K. This shows that a nontrivial amount of emission comes from the bubble volume, especially for the C band. This is an encouraging result, since it implies that if the pressure can be raised enough to get the emission, this type of model will automatically meet the anti-correlation requirement.

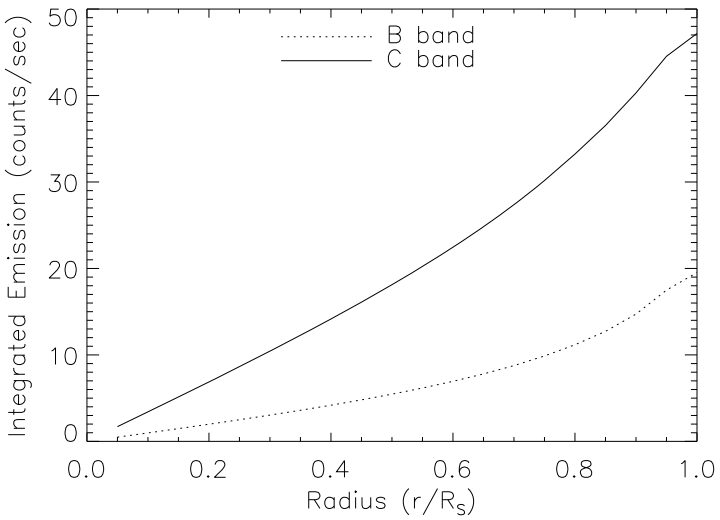

Figure 3.11: Integrated equilibrium B and C band emission over a 100 pc bubble

3.5 Conclusions

This chapter has examined one-dimensional multiple explosion models for the Local Bubble in some detail. The results from the various model runs have significant regularities that are themselves encouraging, since it suggests that the observed uniformity of the X-ray emission across the sky is the result of a conspiracy of physical forces, not initial conditions.

Multiple explosions, widely separated in time, have been shown to create large bubbles easily, without using excessive supernova energy. These bubbles tend to have constant internal pressure and a uniform temperature distribution, and these characteristics can be used to calculate the expected observational parameters such as the X-ray emissivity. The main failure is that the pressure inside the bubbles is too low by a factor of about 1.5 in the

three explosion models and about 2 in the two explosion models. An additional problem is getting the C/B ratio correct, although physically reasonable variations of the thermal conduction flux are likely to be enough to change this.

In general, it seems that a successful model would have $T_c = 1.3 \times 10^6$K or possibly slightly higher to take into account the variation between equilibrium and non-equilibrium emission. Using equation 3.34, it is seen that this can be accomplished by reducing β by a factor of 6 or slightly more. Increasing the bubble pressure, and thus emissivity, is a more challenging task. Since 3 explosion models tend to have higher pressures than 2 explosions, perhaps using 4 or 5 explosions would suffice. Another possibility would be to vary the external ISM pressure, though large changes would be constrained by observations.

Once a successful model with sufficient X-ray emissivity and hardness is found, many other characteristics of the model can be immediately calculated. These include the column densities of observable ions, such as C IV, N V, and O VI, or velocity profiles for lines such as O III 5007Å. These would be testable predictions using either existing data or data from new instruments such as the Wisconsin H-Alpha Mapper (WHAM) or the Spatial Heterodyne Spectrometer (SHS).

Appendix A

Using the 'Odin' Code

A.1 Overview

In order to run the Odin (One Dimensional Interstellar Numerologist) code, a text file containing the initialization parameters must be created and fed to the program. This is done by putting the name of the input file after the program name in the command, as shown here.

```
odin inputfile.inp > inputfile.err &
```

This will result in the program reading the file `inputfile.inp` and all informational messages will be redirected to the file inputfile.err. This file will then contain any messages about unknown commands, as well as the start and stop times of the program as given by the system clock. This is useful for long-term timing of the code.

The allowed commands for the Odin program are given in table A.1. It is possible, however, for more than one program to read the same initialization file, perhaps sharing some values and ignoring others. The Odin program will flag and output as warnings any lines it does not understand in the initialization file. However, it will continue to run as long as the lines it does

understand do not confuse it.

Another feature of the code is that it will create a core dump file for nearly all "severe" errors. The definition of a severe error varies, but in general any condition that would result in either a program crash at some point, or a completely non-physical condition, is considered severe. Note that there is very little checking of the "reasonableness" of the input values. Asking for a magnetic field of 5 gauss (instead of 5μG) will result in an explosion envirorment that is rather stiff.

The core file can usually be deleted if the cause of the crash is known. One common cause is using standard cosmic abundances with dust, which the code knows is impossible, and so it prints an error message and dumps core. Otherwise, the core file can be used with the debuggers `dbx` or `gdb` to investigate the crash. When compiled with `gcc` (the recommended compiler), the code contains the necessary debugging information to allow the user to examine variable values and other information relevant to the crash.

Table A.1: Odin Parameters

Commands	Default	Units	Description
INCELLS	28	–	The number of initial cells
SBANG		Special	See below
SDUST		Special	See below
SDEBUG		Special	See below
SMODIFY		Special	See below
ADD_ZONES	False	–	Add more zones as needed
DBFIELD	0	gauss	Magnetic field strength
DDIMEN	3	–	Dimensionality of system
DGAMMA	5/3	–	Cp/Cv for the medium
DTEMP	10^4	K	Initial gas temperature
DDENS	.1	cm^{-3}	Initial gas density
DDELTAR	.1	pc	Size of the initial cells
DGRAVITY	0.	cm/s^2	Gravitational acceleration
DZETAH	0.	ion/s/H	H photoionizations/s/H atom
DZETAHE	0.	ion/s/H	He photoionizations/s/H atom
THERMAL_COND	None	–	Use thermal conduction
DMOD_COOL	1.0	–	Linear factor for gas emission
DMOD_TC	1.0	–	Linear factor for T.C.
DMOD_T0	0.0	–	Use density dependent T.C.
DTC_COS2	1.0	–	$\cos(T)^2$ factor in T.C.
SABUNDTYPE	A&G	–	Depleted or AndersGrevesse
SCOOLING	None	–	None Kahn Isobaric NonEquil
CHARGE_EXCH	None	–	Use charge excharge
IPLOT	0	–	Plot pressure every N steps
PSEDOV	N	–	Plot sedov radius.
SOUTFILE*	""	–	Output file name
DMAXTIME*	10^7	yr	Model end time
IMAXSTEP*	-1	–	Max. steps to run
IMAX_ZONES	-1	–	Max. number of zones
SCHOPCELLS	N	–	See below
VARYCHI	N	–	Allow χ to vary
ISUBSDETAIL	2		0, 1 or 2 for `.sub` output
DSUBSTIME*	-1	yr	Time between `.sub` reports
DREPTTIME*	-1	yr	Time between `.out` reports
IREPTSTEP*	-1	–	Steps between `.out` outputs
TOTALSAVE	N	–	Save ALL variables in `.out` file
SRESTART*		Special	See below

Table A.2: Explosion parameters

Keyword	Default	Description
DRADIUS	None	Radius of explosion, in pc. Can be anything.
DMASS	None	Mass in explosion,in solar masses
DTIME	None	Time of explosion, in years past initialization
DE51	None	Energy of explosion, in 10^{51} erg units
STYPE	None	Either THERMAL or KINETIC, depending.

A.1.1 Entering an explosion: SBANG

SBANG is used to give parameters for an explosion. It can be followed by one of the subcommands given in Table A.2.

Multiple explosions can be entered by simply putting them in sequence. Note that there are NO default values. In order to be legal, each explosion MUST have a radius, mass, time, energy, and type given.

A.1.2 Dust parameters: SDUST

SDUST – is used to give the dust parameters. Dust can be present everywhere in the model, or only outside the ejecta. This second choice avoids the problem of the dust being instantly destroyed by high temperatures inside the actual explosion. Also, the porosity of the silicate dust can be given, with 0 indicating solid dust and 1.0 being a hypothetical "all-vacuum" dust. However, current code limitations mean that the only two legal values for the dust porosity is 0.0 and 0.8. The complete set of parameters is given in Table A.3

A.1.3 Removing unsightly excess cells: SCHOPCELLS

SCHOPCELLS – Provides instructions to the code as to when it is permissable to drop cells from the calculation. This could happen in many different

Table A.3: Dust parameters

Keyword	Default	Description
Everywhere		Dust everywhere, in ejecta and ISM
OutsideEjecta		Dust only present outside the initial ejecta
None	Yes	No dust in code
NoCooling	Yes	No dust cooling
WithCooling		Dust cooling present
DPOROSITY	0.	Percentage of dust sphere that is vacuum. Legal values 0.0 or 0.8 only.

Table A.4: Chopping parameters

Keyword	Default	Description
DMAXTEMP	2×10^4K	Maximum temperature for backup cells
NBACKCELLS	30	Number of cells to use behind front of zones

circumstances, but the main reason in all cases is that the cells have no effect on the intended results of the calculation and take up substantial extra computational time.

Currently, this is most flagantly obvious in the case of an old supernova explosion. The shock wave will continue indefinitely but weakly; the gas immediately cools after being shocked. So, these cells should be dropped to aid in computations.

The idea is to chop off the shocked zones, so that the cells no longer have a shock at the front. The behavior depends directly on the parameters given below. The code looks at the zones within NBACKCELLS of the last "shocked" zone (a zone where the viscous pressure is more than 10% of the total pressure), and if the temperature in this range never exceeds DMAXTEMP, then this is considered an allowable cutting point.

This code has never been tested. Use at your own risk; it exists mainly as a basis for future modifications.

Table A.5: Non-uniform parameters

Keyword	Units	Description
DRADIUS	pc	Radius to end changes
DDENS	cm^{-3}	New density inside the radius change
DTEMP	K	New temperature inside the radius change
DBFIELD	G	New magnetic field inside the radius change

A.1.4 Non-uniform initial parameters: SMODIFY

SMODIFY – Allows changes to the otherwise-uniform initial conditions. First a "radius" for the changes must be specified with SMODIFY DRADIUS. This radius **must** be larger than any supernova radius given with an SBANG; if not, the code will abort. After this command, the other three commands in Table A.5 can be specified, and will take effect from the first cell after the explosion (or the first cell after a previous SMODIFY DRADIUS) until the specified radius is reached.

Multiple SMODIFY DRADIUS commands can be given to modify the code multiple times at different points. In each case, the density, temperature, or magnetic field changing commands must be given after the radius.

If any of the parameters are *not* given, they will default to the value given initially, in the DDENS or DTEMP or DBFIELD command.

A.1.5 Debugging the output: SDEBUG

This keyword allows the user to get detailed output information from a particular time in the run. The main use is for looking at times right after an explosion, when normally no output would occur for some time. The debugging output is by default simply the state of the hydrodynamic variables,

Table A.6: Debug parameters

Keyword	Units	Description
DSTART	None	Time to start debugging output
DEND	None	Time to finish debugging output
ISTEPS	None	Number of steps to continue debugging
SFILE	""	Optional file for debugging information output

written to the `.out` and `.ion` files every time step, instead of every 100,000 years or whatever DREPTTIME is set to.

A.1.6 Restarting the code: SRESTART

If the SRESTART filename.res command is present in the input file, restart from the file name given in filename. This "restart" file is created from the output file using the program makerestart, which is also part of the Odin package. Parameters marked with a * in table A.1 will be taken from the new input file; all others commands are over-ridden by the save file. Currently, this does not work with ion following.

A.2 Example Initialization file

This is the input file for a series of 3 supernovae, with dust. Included in the file is one line, `SBANDS WISCONSIN` which the Odin code does not understand but will be used by a subsequent program.

```
SOUTFILE M3m_k1d_001
INCELLS 200
ADD_ZONES
DBFIELD 5E-6
```

```
DDIMEN 3
DGAMMA 1.6666666666667
DTEMP 2.2E4
DDENS 0.2
DDELTAR 0.1
DGRAVITY 0.0
SABUNDTYPE Depleted
SCOOLING NonEquil
SDUST Everywhere
SDUST WithCooling
SDUST DPOROSITY  0.0
ISUBSDETAIL 2
THERMAL_COND
DMOD_TC 1.0
DMAXTIME 1.E7
DSUBSTIME 3.E4
DREPTTIME 3.E5
SBANG DRADIUS 1.0
SBANG DMASS 2.0
SBANG DTIME 0.0
SBANG DE51 0.5
SBANG STYPE KINETIC
SBANG DRADIUS 1.0
SBANG DMASS 2.0
SBANG DTIME 1.E6
```

```
SBANG DE51 0.5
SBANG STYPE KINETIC
SBANG DRADIUS 1.0
SBANG DMASS 2.0
SBANG DTIME 3.E6
SBANG DE51 0.5
SBANG STYPE KINETIC
SBANDS WISCONSIN
```

Appendix B

Using 'Odin' Utilities

B.1 Utility programs

Odin can output only three types of files:

- `.out` : An HDF file containing the hydrodynamic variables
- `.sub` : An ASCII file containing some calculated values, such as total energy and equilibrium emission
- `.ion` : An HDF file containing the ionic abundances for each cell

These files can then be used to generate many other types of data. The `.out` and `.sub` files are mainly read by IDL routines, which are not described here. However, the `.ion` files need further processing before they can be used to compare against observations. The following programs provide that processing.

There are three utility programs that can be used, all of which use the same format for input (`.inp` files). They are listed in Table B.1:

Table B.1: Utility Programs

Program	Description
spectrum	Calculates the emitted spectrum for the given ionic abundances in the `.ion` file. Can output an XSPEC table model, and HDF file containing the entire spectrum, or ASCII files with the Wisconsin band rates or another arbitrary binning.
set_etandu	Using the HDF spectrum file generated by spectrum, calculates the surface brightness of the emitting remnant for a given size on the sky.
calc_emis	Creates a `.ion` file using equilibrium ionization, which can then be used to test the other two codes against XSPEC built-in models.
opt_line	Using the `.ion` file data, calculates the shape of various spectral lines in the data.

B.2 Running spectrum

In order to run the code, a text file containing the initialization parameters must be created and fed to the program. This is done by putting the name of the input file after the program name in the command, preceeded by a <. Optionally, a > followed by another file name can be used to collect all error messages which will otherwise be written to the screen. For example,

```
wisp5> spectrum < filename.inp > filename.ser
```

will run the `spectrum` program, using `filename.inp` as the input command file, and directing all messages (both informative and error messages) to the file `filename.ser`.

The commands that will have an effect on the program are shown in the following table. Commands not in this list will result in an informational error message, but the program will run with no problems; this means that it is

Table B.2: Spectrum Parameters

Commands	Default	Units	Description
SOUTFILE	""	–	Name of output file
INBIN	1000		Number of bins, in energy units
FBINMIN	45	eV	Minimum bin, using energy units
FBINSYZ	1	eV	Bin width, in eVs, using energy units
SBANDS			WISCONSIN HARD XSPEC FULL
SABUNDTYPE	A&G	–	Depleted AndersGrevesse Allen

Table B.3: Band parameters

Keyword	Default	Description
WISCONSIN	N	The B and C band count rates, in SOUTFILE.wis
HARD	N	The hard band count rates, in SOUTFILE.hrd
XSPEC	N	Spectra in XSPEC format, in SOUTFILE.tbl
FULL	N	All spectra in all cells, in HDF format, in SOUTFILE.spe

entirely possible, and in fact useful, to have all commands for a given model in a single .inp file, which is submitted to many different programs in turn.

B.2.1 Output bands: SBANDS

SBANDS – is used to say which bands the spectrum should be output in. There are currently 4 possible choices, as shown in the following table, which will output:

The "HARD" bands are binned in the following way: < 100 eV, 0.1 to 1 KeV, 1 to 4 KeV, and > 4 KeV. Multiple SBANDS may appear; the code will do them all.

Table B.4: calc_emis parameters

Keyword	Default	Description
SOUTFILE	""	Name of output file
SABUNDTYPE	A&G	One of: Depleted AndersGrevesse Allen
DDENS	1.	The density of nuclei, in cm^{-3}.
DTSTART	5	Start temperature, in K or log(K).
DDELTAT	.1	Temperature spacing, in K or log(K).
ITSTEPS	10	The number of temperature steps to take.
LINEART	N	Linear temperature steps; else do log.
ICELLS	10	Number of fake "cells" to write out.
DDELTAR	.1	The delta radius of the cells, in parsecs.

B.3 Running calc_emis

The calc_emis program (see Table B.4) is meant to be used as a testbed for other programs in the utility package. It uses the Raymond & Smith code in equilibrium mode, to generate a .ion file which can be read by the spectrum code. Each "saved timestep" in this case is a different equilibrium temperature, and has a number of cells (given by ICELLS) at varying radii, which all have that temperature. Temperature stepping can be either linear (if LINEART is present), in which case DTSTART and DDELTAT are in Kelvin, or power-law, in which case DTSTART and DDELTAT should be the log base 10 of their actual value.

B.4 Running set_etandu

The set_etandu program (see Table B.5 is designed for use with the XSPEC program. The Einstein SSS, for example, has only a 3 arc-minute field of view, which for galactic SNR will often be smaller than the full size of the remnant. As a partial method of dealing with this problem, the set_etandu program

Table B.5: set_etandu parameters

Keyword	Default	Description
SOUTFILE		Name of input/output file, no extension
SMODELNAME		Name of the model in XSPEC
FETANDU		Radius to sum over, in parsecs.
FBINMIN		Minimum bin (in eV), using energy units
FBINSYZ		Bin width, in eVs, using energy units

will take a parameter FETANDU, which is given in parsecs, and calculate the emission from the remnant from inside that distance. The program effectively calculates the surface brightness from the remant inside the FETANDU value, and then sums over that portion of the remnant to get the total emission. The result is an XSPEC table model with the suffix .red appended.

B.5 Running opt_line

The opt_line program (see Table B.6) was written to allow comparisons with observed line profiles, specifically those from OIII, CIV, SiIV, NV, and OVI, among others.

The program reads the input file, which can contain up to 20 different lines to output, each with their own Δv, v_{max}, and v_{min}. The line list is restricted, however; currently, the only lines that can be observed are: He II(1640Å), C III (1910Å), C IV (1549.1Å), O III (1662Å), O III (5007Å), O IV (1402Å), S IV (1390Å), Fe X (6379Å), Fe XIV (5303Å), O VIII (653.61Å), and O VI(1033.80Å). This list can be easily extended to any line in the Raymond & Smith line list by a simple modification to the program.

Currently, the program requires the `INSIDE` command. Code to handle observing a remnant from the outside exists in the program, but it has not been

Table B.6: opt_line parameters

Keyword	Default	Description
SOUTFILE	None	Name of input/output file, with no extension
SABUNDTYPE	A&G	One of: Depleted AndersGrevesse Allen
FLINE	None	Wavelength of line to output, in angstroms
FDELTAV	5.	Resolution desired for current line, in km/s
FMAXV	100.	Maximum positive velocity doppler shift
FMINV	-100.	Maximum negative velocity doppler shift
INSIDE	True	Assume the observer is inside the remnant, looking out

tested or run due to time constraints. Getting the code to run for an external bubble should not be particularly difficult, however. One other limitation is that the total resolution is limited to 100 bins; thus (v_{max} - v_{min})/$\Delta v < 100$. This can be easily changed by recompilation with a new value for the MAXRES parameter.

B.6 Examples

The following are example input files. The first was named `w44_neq_003.inp` and simulates the SNR W44, outputing an XSPEC table model to compare against the data from the Einstein SSS.

```
SOUTFILE  W44_neq_003
DREPTTIME  2.e3
DSUBSTIME  2.e2
DMAXTIME 5.e4
ISUBSDETAIL 2
ADD_ZONES
INCELLS 200
```

```
DBFIELD  5.E-6

DDIMEN  3.0

DDELTAR 0.1

DGAMMA  1.666666666666666666

THERMAL_COND

DMOD_TC 1.0

DTEMP  1.e4

DDENS  2.5

SBANDS WISCONSIN

SBANDS HARD

SBANDS  XSPEC

SBANDS  FULL

INBIN 1000

FBINMIN 45

FBINSYZ 5

FETANDU 2.616

SABUNDTYPE AndersGrevesse

SCOOLING NonEquil

CHARGE_EXCH

SBANG DRADIUS 2.0

SBANG DMASS 2.0

SBANG DTIME 0.0

SBANG DE51 0.5

SBANG STYPE THERMAL
```

This file, called `constantT.inp` was used to create a table model of the Raymond & Smith model that is already built into XSPEC. Comparing the results against the built-in code showed that the two methods agree to within .1% in temperature.

```
SOUTFILE constantT
DDENS 1.0
DTSTART 5
DDELTAT .1
ITSTEPS 20
ICELLS 100
DDELTAR .1
SABUNDTYPE AndersGrevesse
SBANDS    FULL
FBINMIN 45
FBINSYZ 5
INBIN 1000
FETANDU 5.0
```

Appendix C

Using the IDL analysis routines

C.1 Overview

Most of the actual data analysis is done using the Interactive Display Language (IDL). This program contains both a Fortran-like language and a comprehensive set of plotting routines. As detailed below, there are a number of files that contain IDL functions and procedures, that are used to read and examine data output by `Odin` or its utility programs. Most of these files, as well as some other necessary definitions, are loaded at startup of IDL by a call to the batch file start.pro.

Many of the output files are in HDF (Hierarchical Data Format), a data format designed at the National Center for Supercomputing Applications at the University of Illinois Urbana-Champaign. The HDF files contain timeslices of the data, which can be accessed in any order. Each slice has an index associated with it, starting at 1 and extending to the last slice in the file. There is a consistent interface for reading HDF files into IDL; first, the file is "opened" for reading, at which point the maximum value of the index will be printed. Then a particular slice can be read into the "working space" of predefined common blocks by a "read" command, which varies for the different

files. All the data read from an HDF is stored in common blocks, so no variables need be remembered.

C.2 Commands

The following files contain procedures used to read data output from `Odin` (`.out`, `.sub`, and `.ion` files) or the utilities (`.spe`, `.wis`, `.hrd`, and `.opt` files) into the IDL workspace.

C.2.1 Analyzing .tbl files

`readXSPEC.pro` contains procedures to read XSPEC table models, used in XSPEC version 8. Version 9 of the XSPEC code now uses FITS format files for this purpose, so the following will soon be obsolete. However, there is a program in the new XSPEC distribution to convert from the old format to the new, so the hydrocode will not be immediately updated, and this routine may still be useful. The main routine is `Read_XSPEC`, which is called as:

```
Read_XSPEC,filename,parms,data
```

`filename` is the name of the XSPEC table model. `parms` and `data` are structures containing the table parameters and data, respectively. The program also uses the following routines to help read the file; they are not designed for independent use but can be helpful if debugging is needed:

```
Read_XSPEC_data,lun,MAXPVALS,numparm,numbin,parms,data
Read_XSPEC_user,lun,addrec
Read_XSPEC_energy,lun,numbin,reclen,parms
```

```
Read_XSPEC_param,lun,MAXPVALS,reclen,numbin,numparm,parms
Read_XSPEC_header,lun,reclen,bytperrec,numbin,numparm, ...
Test_XSPEC_table,filename,result
```

C.2.2 Analyzing .hrd files

The `spectrum` program will create a `.hrd` file when given an input code `SBANDS HARD`. The `.hrd` is an HDF file which contains the band emission for each parcel, integrated over 4 (rather randomly chosen) bands: less than 0.1 keV, 0.1 – 1.0 keV, 1.0 – 4.0 keV, and greater than 4.0 keV. The `readbands.pro` file contains procedures used to read and plot a `.hrd` file. The routines are:

- `OpenBands,file` – Opens a `.hrd` file for reading.
- `ReadBands, reference` – Reads a single saved band spectrum into the IDL workspace. If `reference` is given, it gets the band spectrum for that index; if it is omitted, it reads the subsequent band spectrum from the current.
- `PlotBands,NH` – Plots the band spectra as a function of radius. If `NH` is given, the bands are plotted assuming it has traveled through the given column density of hydrogen (assuming an average σ for each band).
- CalcFlux – Calculates the total flux in each band for the current time.

C.2.3 Analyzing .spe files

The `spectrum` program creates `.spe` files in response to the input code `SBANDS FULL`. The `.spe` file is an HDF file that contains the entire spectrum for

each zone and timestep (and is thus rather large). There are three IDL files that deal with these kinds of files: `readfull.pro`, `analyze_full.pro`, and `sum_spec.pro`. The `readfull.pro` file contains the procedures necessary to open and read the `.spe` files:

- `openfull,file` – Opens a `.spe` file for reading.
- `readfull,reference` – Gets a single spectrum, with the index given by the `reference` parameter. If `reference` is absent, the next (time-ordered) spectrum is read.

The `analyze_full.pro` file has two procedures to analyze the spectral data:

- `SB_full,surf` – Returns in the `surf` variable an array which contains the surface brightness versus impact parameter for the current spectrum
- `Bin_full,nh,radius,surf,bindata` – Bins the surface brightness `surf` into 5 bands, the first 4 of which are the same as the `.hrd` file, and the last all emission in the .2 – 2.2 keV range. `nh` is the foreground hydrogen column density, and `bindata` the result of binning the surface brightness `surf`.

The `sum_spec.pro` file has two procedures and a function to analyze the spectral data:

- `FUNCTION tot_spec` – Prints out the total emission from the remnant, in ergs/sec.
- `sum_spec,result` – Upon return, `result` is an array containing the total emitted spectrum from the remnant.

- `emit_spec,result` – Reads each of the datapoints in the .spe file, calculating the total emission at each time, and returns in `result` a 2xN array of the time and emission for the spectrum file.

C.2.4 Analyzing .ion files

The `.ion` files are created by the hydrocode itself, when run in the NonEquil mode. The `.ion` file is an HDF file, storing all the ion concentrations for each zone and timestep. Although the `.ion` file is used mostly by the `spectrum` program to calculate spectra, there are two IDL files that can use it directly: `readions.pro` and `column_den.pro`. The `readions.pro` file contains the following procedures:

- `openion,file` – Opens a `.ion` file for reading
- `readion,reference` – Reads the given index `reference` from the `.ion` file. If `reference` is not given, reads the data from the next timestep.
- `calcion,z` – Calculates the mean ion charge for the atoms for each zone and returns them as an array in `z`.
- `plotion` – Plots, versus radius, the average ion charge for the standard 12 atoms as well as the temperature and density.
- `splotion` – Plots, versus radius, the average ion charge for carbon and iron as well as temperature and density.

The `column_den.pro` file contains procedures to calculate the column densities of various ions directly.

- `do_colden,result` – Calculates the column densities of hydrogen and 5 ions: C IV, N V, O VI, Si IV, and Si III, which are returned in the array `result`.

- `plot_colden,result` – Uses the `result` array returned from `do_colden` to plot the column densities for the ions.

C.2.5 Analyzing .opt files

The `.opt` file is created by the `opt_line` program, using the `.ion` file created by the hydrocode. The `.opt` file is an HDF file, containing the emission from each of the requested optical lines for each parcel and timestep from the run. There are two files that deal with `.opt` files: `readopt.pro` and `set_optplot_size.pro`. The `set_optplot_size.pro` file contains only a single function that sets the plot size used by the `readopt.pro` programs, so is not used directly. The `readopt.pro` file contains the following routines:

- `openopt,file` – Opens a `.opt` file for reading.

- `readopt,reference` – Reads the given index `reference` from the `.opt` file. If the index `reference` is not given, reads the data from the next timestep.

- `plotopt` – Plots the line data for all the lines in the `.opt` file.

- `oplotopt` – Overplots the line data from the current selection of the `.opt` file over whatever previous data has been plotted. Used to show how the data is changing.

Analyzing .out files

The `.out` file contains the hydrodynamic variables from a given run, such as the temperature, density, pressure, and so on. There are a number of procedures to analyze this data, the first of which are contained in the file `readslice.pro`. This contains two procedures to open the `.out` file and read it:

- `fo,file` – Opens a `.out` file for reading.
- `rs, reference` – Reads a single timestep from the `.out` file. If the index `reference` is given, that index is read; otherwise the next timestep is read.

The `calc_bands.pro` file contains programs to calculate the equilibrium emission from the temperature and density distribution of the current selection.

- `read_eqbands` – Reads the equilibrium count rates per emission measure file; this is automatically called at the first call to `plot_eqbands`.
- plot_eqbands,maxpc – Using the current selection of the `.out` file, plots the B and C counts/sec vs radius. If `maxpc` is included, the plot is from 0 to `maxpc`; if not, the maximum radius of the actual data is used.

There are three files which contain plotting procedures. The main file is `scan.pro`, and it has variants `oscan.pro` and `dscan.pro`. All create plots of six important variables versus radius.

- `Scan,radius` – Plots the density, temperature, velocity, pressure, emission (lin-log), and adiabat versus radius. If `radius` is given, the plot

extends from 0 to `radius`; otherwise, the default radius is the position of the last cell in the selection.

- `logscan,radius` – Similar to `scan`, except uses lin-log plots for density, temperature, pressure, and adiabat.
- `scanpt,radius` – Similar to `scan`, except plots individual points instead of connecting them with line segments.
- `logscanpt,radius` – Combines the effects of `logscan` and `scanpt`
- `oscan` – Overplots the current selection against the previously plotted (with `scan`) data. Used to show the evolution of the hydrodynamic variables.
- `ologscan` – Similar to `oscan`, except for `logscan`
- `oscanpt` – Similar to `oscan`, except for `scanpt`
- `ologscanpt` – Similar to `oscan`, except for `logscanpt`
- `DScan` – This procedure creates a plot similar to `scan`, except it plots the total dust cooling, the silicate and graphite fractions destroyed, the gas temperature, and the silicate and graphite mass densities.
- `Dlogscan` – Similar to `scan` using a lin-log format.
- `Dscanpt` – Similar to `scan` using points instead of line segments
- `Dlogscanpt` – Combines the effects of `dlogscan` and `dscanpt`

The `dem.pro` file contains the procedures necessary to calculate the differential emission measure ($n_e^2 dr/dT$) and compare the result against the analytical expectation.

- `FUNCTION dem_theory,nt` – This function is called from `dem`; it calculates the expected DEM for the given pressure nt.
- `FUNCTION avecell,c1,c2` – This routine is called from `scell`; it averages each pair of cells to remove jitter.
- `dem,PLOTTYPE=pt,BETAMOD=beta` –
- `scell,acell` – This routine is called from `dem`, to smooth the cells of numerical jitter.

The `fit_temp.pro` file fits the temperature profile to a function of the form $T(r) = T_c(1 - (r/R_s)^{a_1})^{a_2}$.

- `do_fits,result,do_len` – This is the main fitting routine. Assuming a `.out` file is open, it loads each timestep in order, and performs a fit to the temperature structure, showing each fit in order. It then finishes by making a plot similar to the one described in `make_fplots` below.
- `make_fplots,result` – When called with the `result` returned from `do_fits`, this procedure plots the values of a_1, a_2, T_c, and R_s versus time.
- `FUNCTION fitfunct,x,t` – This function is called from `do_fits` to fit the cell data to the above function.

- `TCfunct,x,a,f,pder` – This routine is called by the function `fitfunct` to evaluate the function.

C.2.6 Analyzing .sub files

The `.sub` file is an ASCII text file created by the `Odin` code directly, and contains various subsidiary information such as the total energy in the system, count rates in various band passes, and the size and energy in the hot bubble. This information is often the most useful, since it can show the entire run at a glance. There are two files that deal with `.sub` files: `readsub.pro` and `colmag.pro`. The `readsub.pro` file contains the following programs:

- `Readsub,filename,results` – Reads the filename and places the results into the `results` array.

- `Eplot,results` – Extracts from the `results` array the energy information, and plots it as a function of time, showing total, kinetic, thermal, radiated, and magnetic energy.

- `HotMass,results,level` – Extracts from the `results` array the information on the hot bubble, and plots it, showing the bubble radius, mass, number of zones, and the kinetic, thermal and magnetic energy in the bubble versus time. The `level` variable can be omitted, in which case the bubble is defined as that region above 10^5K. If `level` is 1, the minimum temperature is 5×10^4K, and if `level` is 2, $T_{min} = 10^4$K.

- `LogHotMass,results,level` – Similar to `HotMass`, except plots in lin-log form.

The `colmag.pro` contains procedures to examine the equilibrium band emission data stored in the `.sub` file, as follows:

- `Colmag,results` – Using the `results` array returned from `readsub`, plots the equilibrium C emission versus equilibrium C/B ratio.
- `Rcolmag,results` – Same as `Colmag`, except limits the range on the X and Y axes.
- `Ocolmag,results` – Same as `Colmag`, except overplots the current value from `results` over the previously plotted values.
- `Bandplot,results,full` – If `full` is omitted, plots strip charts of the B and C band rates versus time. If `full` is given, then plots all the calculated rates: B, C, Be, B', M1, and M2.
- `FUNCTION dolog,array` – Used by the `ColorStrip` procedure; it calculates whether or not to plot the data in linear or log form, depending on the range in the data.
- `ColorStrip,results,short` – A fancier version of `Bandplot`, which includes names on the axes and will work with `.wis` data arrays as well. The (integer) value of `short` determines the number of plots that are given, from 1 to 6; the order is predetermined, however, to be the same as shown in `Bandplot`.

C.2.7 Analyzing .wis files

The `.wis` file is an ASCII text file created by the `spectrum` program, when it is called with the `SBANDS WISCONSIN` input. It contains the actual count rates

for the various Wisconsin bands, calculated by running the Raymond & Smith (1993) code to generate the spectrum and then folding that through the band responses. The `readwisc.pro` file contains procedures for dealing with this data, as shown below.

- `ReadWisc,filename,wisc` – Reads the `.wis` file and places the result into the array `wisc`, simultaneously printing out the structure of the array.

- `AdvReadWisc,filen,result` – An advanced form of the `ReadWisc` program. This takes a filename `filen` *with no extension* and then appends the `.wis` extension to read the `.wis` data and appends the `.out` extension and reads the entire `.out` file, calculating as it goes the bubble radius and average pressure.

- `Plotwisc,result` – This procedure takes the `result` from `AdvReadWisc` routine and plots the values of the B and C emission, as well as B/p^2R_s and C/p^2R_s versus time.

- `Plotpr,result` – Similar to `Plotwisc`, but the third and fourth plots are of the average pressure and the bubble radius, respectively.

- `CmpRates,wisres,subres,num` – This routine takes the resultant array `wisres` from the `ReadWisc` procedure and the array `subres` from the `Readsub` procedure, and plots a comparison between the equilibrium count rates in the `.sub` file and the actual count rates in the `.wis` file. If `num` is given, then only `num` plots are made; otherwise, plots are made for each band.

C.3 General Analysis Routines

There are also some procedures written that do not deal directly with the `Odin` code output, but instead calculate useful values using IDL alone. There are two files in particular, `absorbX.pro` and `bandrates.pro`, which contain such procedures. The first, `absorbX.pro`, contains the following:

- `ReadMMdat` – Reads the `morrison.dat` file.
- `Find_sigmas` – Calculates the average cross section for the bands used in the `.hrd` file.
- `Function sigma,E` – Calculates the actual cross sections `sigma` for the given energy(s) `E`.
- `morrison.dat` – The cross sections σ for the ISM, from the Morrison & McCammon (1983) paper.

This next file, `bandrates.pro`, contains programs to calculate the equilibrium emission of a bubble with a temperature distribution of the form

$$T(r) = Tc(1 - r^{a_1})^{a_2} \tag{C.1}$$

- `Function T,r` – Returns the calculated value of T(r).
- `Function b,t` – Returns the calculated value of B(T), the equilibrium count rate per emission measure at temperature T.
- `Function c,t` – Same as above, for the C band.
- `function bfunc,r` – Calculates the actual B band emission, using the density information passed in a common block.

- `function cfunc,r` – Same as above, for the C band.

- `plot_emis,Tcentral,Rs,pressure` – Given a central temperature, bubble radius, and pressure, this procedure plots the resultant emission in the B and C bands, and prints out the total emission.

- `calc_rates,barr,carr` – Calculates the emission in the B and C bands for a range of central temperatures and radii. The bubble is assumed to be 100 pc in size, and the radii vary from considering only 5% to 100% of this radius. The `barr` and `carr` arrays contain the B and C values, respectively.

- `vary_rates,barr,carr,varr` – Calculates the B and C count rates and the C/B equilibrium ratio (`barr`, `carr`, and `varr`, respectively) for a range of parameters a_1 and a_2 and a range of central temperatures.

- `c_vary_rates,varr` – Using the result `varr` returned from `vary_rates`, creates multiple contour plots showing the changes for different values of a_1 and a_2.

C.4 Miscellaneous IDL code

C.4.1 Initialization

Nearly all of the above programs are initially compiled into the IDL working space by the batch file `start.pro`. This file should be executed at startup with the command `IDL> @start`. It contains all the necessary definitions for common blocks and all the necessary compilation instructions.

C.4.2 Overplotting

While IDL contains code to overplot figures, and code to plot multiple images per page, the two cannot be combined without using extra code. This code is provided in the `multi_oplot.pro` file, as described below.

- `store_moplot,p_store` – This procedure stores the information necessary to perform overplots when using multiple plots per screen. It is called after every plot, and then its companion can be used to restore the settings for that plot.

- `restore_moplot,p_store,i` – This procedure restores the plot values so that an overplot command in IDL will work correctly.

C.4.3 Making images

There are two files which contain procedures used to make images out of one-dimensional plots: `surface_brightness.pro` and `formimage.pro`. Their respective contents are described below:

- `FUNCTION SB,r,f` – Calculates the surface brightness, assuming there is a spherical bubble with zones given by the `r` vector, and the emission in each zone given by `f`.

- `FormImage,r,f,image,BOUNDARY=bound,NOLIMIT=nolim` – Creates an image `image`, using the surface brightness routine (which uses the same `r` and `f` vectors. Setting the `BOUNDARY` parameter to a non-zero value puts a bright circle at the edge of the created image; setting the `NOLIMIT` parameter allows arbitrarily large images to be created. If `NOLIMIT` is

not set, vectors larger than 200 elements are rejected and binning is recommended.

C.4.4 Automatic Routines

These files do not contain any procedures or functions, but are rather simply lists of IDL commands, executed in batch mode. They are run by typing at the command line `IDL> @filename.pro`. Each was written to output a series of specially designed plots, and so are not very general. They are included here as examples.

- `a_bandrates.pro` – Make plots of equilibrium emission
- `a_columnden.pro` – Make plots of column densities for various `Odin` runs.
- `a_fit_temp.pro` – Runs the `do_fits` procedure on a selection of `Odin` runs.
- `a_overview.pro` – Assumes that `filename` is set to the name of an `Odin` run with no extension, and runs a number of standard routines to give an overview of the data.
- `a_plotpr.pro` – Runs `plotpr` on selected `Odin` runs.
- `a_plotwisc.pro` – Runs `plotwisc` on selected `Odin` runs.

References

1. Arnaud, K. 1995, "XSPEC: An X-Ray Spectral Fitting Package"

2. Baxter, A. J., Wilson, B. G., Green, D. W. 1969, ApJ, 155, L145

3. Bloch, J. J., Jahoda, K., Juda, M., McCammon, D., Sanders, W. T., Snowden, S. L. 1986, ApJ, 308,L59

4. Bloemen, J. B. G. M. 1987, ApJ, 322, 694

5. Bowyer, C. S., Field, G. B., & Mack, J. E. 1968, Nature, 217, 32

6. Breitschwerdt, D. & Schmutzler, T. 1994, Nature, 371, 774

7. Bunner, A. N., Coleman, P. L., Kraushaar, W. L., McCammon, D., Palmieri, T. M., Shilepsky, A., & Ulmer, M. 1969, Nature, 223, 1222

8. Burrows, D. N., McCammon, D., Sanders, W. T., Kraushaar, W. L. 1984, ApJ, 287, 208

9. Burrows, D. N. & Mendenhall, J. A. 1991, Nature, 351, 629

10. Burrows, D. N. & Mendenhall, J. A. 1994, AIP Conference 313, p.16

11. Cowie, L. L. & McKee, C. F. 1977, ApJ, 211, 135

12. Cowie, L. L. 1977, ApJ, 215, 226

13. Cox, D. P. & Anderson, P. R. 1982, ApJ, 253, 268

14. Cox, D. P. & Reynolds, R. 1987, ARA&A, 25, 303

15. Cox, D. P. & Smith, B. W. 1974, ApJ, 189, L105

16. Cox, D. P. & Snowden, S. L. 1986, Adv. Space Res., vol 6, no 2, p 97

Diamond, C. J., Jewell, S. J., & Ponman, T.J. 1995, MNRAS, 274, 589

17. Edgar, R. J. 1993, personal communication

18. Edgar, R. J., & Cox, D. P. 1993, ApJ, 413, 190

19. Fabian, A. C. & Barcons, X. 1992, ARA&A, 30, 429

20. Fried, P. M., Nousek, J. A., Sanders, W. T. & Kraushaar, W. L. 1980, ApJ, 242, 987

21. Garmire, G. P. *et al.* 1992, ApJ, 399, 694

22. Giacconi, R. *et al.* 1962, Phys.Rev.Lett, 9, 439

23. Henry, R. C., Fritz, G., Meekins, J. F., Friedman, H., & Byram, E. T. 1968, ApJ, 153, L11

24. Jahoda, K. M., McCammon, D., Dickey, J. M., & Lockman, F. J. 1985, ApJ, 290, 229

25. Jenkins, E. B. & Meloy, D. A. 1974, ApJ, 193, L121

26. Jenkins, E. B. 1978a, ApJ, 219, 845

27. Jenkins, E. B. 1978b, ApJ, 220, 107

28. Jenkins, E. B. 1978c Comments Astr., 7, 121

29. Juda, M., Bloch, J. J., Edwards, B. C., McCammon, D., Sanders, W. T., Snowden, S. L., & Zhang, J. 1991, ApJ, 367, 182

Kahn, F. D. 1975, Proc. 15th International Cosmic Ray Conference (Munich), 11, 3566

Kahn, F. D. 1976, A&A, 50, 145

30. Marshall, F. J. & Clark, G. W. 1984, ApJ, 287, 633

31. Marshall, F. E., Boldt, E. A., Holt, S. S., Miller, R. B., Mushotzky, R. F., *et al.* 1980 ApJ, 235, 4

32. McCammon, D. & Sanders, W. T. 1990, ARA&A, 28, 657

33. McCammon, D., Bunner, A. N., Coleman, P. L., Kraushaar, W. L. 1971, ApJ, 168, L33

34. McCammon, D., Burrows, D. N., Sanders, W. T., & Kraushaar, W. L. 1983, ApJ, 269, 107

35. McKee, C. F. & Ostriker, J. P. 1977, ApJ, 218, 148

36. Miller, W. W. III 1994, PhD Thesis

37. Morrison, R. & McCammon, D. 1983, ApJ, 270, 119

38. Paresce, F. 1984, AJ, 89, 1022

39. Raymond, J. C. & Smith, B. W. 1977, ApJS, 35, 419.

40. Raymond, J. C. 1993, personal communication

41. Richtmyer, R. D., & Morton K. W. 1967, *Difference Methods for Initial Value Problems*, 2nd ed. (New York: Wiley-Interscience)

42. Sanders, W. T., Kraushaar, W. L., Nousek, J. A. & Fried, P. M. 1977, ApJ, 217, L87

43. Sanders, W. T. & Edgar, R. J. in "Proceedings of IAU Conference #152", in press.

44. Sedov, L. I. 1959, *Similarity and Dimensional Methods in Mechanics*, (New York: Academic Press)

45. Shelton, R. L., & Cox, D. P. 1994, ApJ, 434, 599

46. Shu, F. H 1992, *The Physics of Astrophysics: Gas Dynamics*, (Mill Valley: University Science Books)

47. Slavin, J. S. 1989, ApJ, 346, 718

Slavin, J. S. & Cox, D. P. 1992, ApJ, 392, 131

48. Smith, R. K, Krzewina, L. G., Cox, D. P., Edgar, R. J., & Miller, W. W. 1995, ApJ, submitted

49. Snowden, S. L., Cox, D. P., McCammon, D., & Sanders, W. T. 1990, ApJ, 354, 211

50. Snowden, S. L., Mebold, U., Hirth, W., Herbstmeier, U., & Schmitt, J. H. M. M. 1991, Science, 252, 1529

51. Snowden, S. L., McCammon, D., & Verter, F. 1993, ApJ, 409, L21

52. Snowden, S. L., McCammon, D., Buurrows, D. N, & Mendenhall, J. A. 1994a, ApJ, 424, 714

53. Snowden, S. L., Hasinger, G., Jahoda, K., Lockman, F. J., McCammon, D., & Sanders, W. T. 1994b, ApJ, 430, 601

54. Snowden, S. L., Freyberg, M. J., Plucinsky, P. P., Schmitt, J. H. M. M., Trümper, J., Viges, W., Edgar, R. J., McCammon, D., & Sanders, W. T. 1995, ApJ, 454, 643

55. Spitzer, Lyman Jr. 1956, *Physics of Fully Ionized Gases*, (New York: Interscience), p. 87

56. Trümper, J. 1983, Adv. Space Res., 2, No. 4, 241

57. Warwick, R. S., Barber, C. R., Hodgkin, S. T., & Pye, J. P. 1993, MNRAS, 262, 289

58. Williamson, F. O., Sanders, W. T., Kraushaar, W. L., McCammon, D., Borken, R., Bunner, A. N. 1974, ApJ, 193, L133